理學博士 學位論文

투과전자현미경 기법을 이용한 다중양자우물의 조성 및 변형의 정량적 분석

Quantitative Analysis of Composition and Strain in InGaN/GaN Multi-quantum wells by Transmission Electron Microscopy Techniques

指 導 交 綏

張 志 豪

2016年 8月

韓國海洋大學校 大學院

應用科學科

半導體物理專攻

趙 英 志

本 論文을 趙英志의 理學博士 學位論文으로 認准함

위원장 안 지 훈 (인)

위 원 장 지 호 (인)

위 원 김 정 창 (인)

위 원 양 민 (인)

위 원 양 준 모 (인)

2016년 8월

한국해양대학교 대학원

Contents of this thesis

Chapter 2 Experiments

Chapter 3 Observation of Microstructure of Light Emitting Diodes

Figure list

Table list

국 문 요 약

본 논문에서는 상용 Light Emitting Diode (LED) 샘플에 적용된 InGaN/GaN 다중양자우물의 조성과 응력을 분석하기 위한 방법으로 투과전자현미경의 여러 기법 중 High-resolution transmission tem (HRTEM), High-angle annular dark-field scanning TEM (HAADF-STEM), Dark-field electron holography 을 제시하였고, 그 기법들을 통해 실제 분석을 진행하고 이를 통해 얻어지는 정보의 정확성과 적용 한계에 관하여 고찰하였다.

이 논문의 목적은 기존에 사용되었던 분석방법들로는 나노미터 단위의 두께를 갖는 다중양자우물 구조를 분석하기에는 공간 분해능이 충분하지 않고, 특히 최근 결정성장 기술의 발전으로 인해 복잡해진 LED 구조에 있어 결함이나 조성, 변형 등의 문제점들의 원인 파악이 힘들어짐에 따라 원자 단위 분해능을 가진 투과전자현미경에 새롭게 도입된 기법들을 다중양자우물의 여러 특성 중 특히 조성과 스트레인의 분석에 적용할 때 그 정확성과 한계에 관해서 고찰하는데 있다.

본 논문은 총 6장으로 구성되어 있으며 각 장의 내용은 다음과 같다. 제 1장에서는 GaN를 기반으로 한 LED의 발달 및 그 중요성

과, LED의 활성층으로 사용되는 InGaN/GaN 다중양자우물의 특성 및 문제점들에 대하여 설명하고 이 논문의 목적을 소개하였다. 제 2장에서는 연구에 사용된 샘플에 대한 설명 및, 본 연구에서 사용된 분석 방법인 RBS, XRD, TEM 등의 분석 원리에 대하여 정리하였으며, TEM 분석을 위한 시편 제작 방법에 대해 설명하였다. 제 3장은 본 논문에서 사용한 상용 LED 시료의 기본적인 결함 분포 등에 대한 정보를 정리하였다. 기판 근처 계면의 미세구조 및 결함의 전파 상황에 대해 분석하고 고찰하였다. 제 4장에서는 다중양자 우물의 Indium 조성을 분석하였다. HRTEM과 HAADF-STEM 방법으로 Indium 조성과 그 분포를 확인하고 고찰하였다. 제 5장은 Dark-field electron holography 방법을 사용하여 다중양자우물의 변형과 그 분포를 분석하고 고찰하였다. 마지막으로 제 6장에서는 본 논문에서 얻은 결과를 정리하여 결론을 기술하였다.

Abstract

In this thesis, HRTEM, HAADF-STEM and Dark-field electron holography, the techniques of TEM methods, were suggested to analysis InGaN/GaN MQWs in the LED. And the indium composition and strains in the InGaN/GaN were investigated by these techniques. The previous analysis methods were difficult to analyze indium composition and strain in the InGaN/GaN MQWs because structure of LED has become more complex and miniaturized. Therefore the purpose of this thesis is to investigate of InGaN MQWs by TEM techniques and discuss about accuracy of indium composition and strain analysis.

In the chapter 1, the history of GaN-based LED, the properties and problems of InGaN/GaN MQWs which used as an active layer are introduced. In the chapter 2, the experiment samples information and analysis methods used in this thesis, which are RBS, XRD and TEM are introduced. And the process of specimen preparation for TEM measurement is explained. In the chapter 3, microstructures of GaN/Al_2O_3 interface and dislocation distribution are investigated. In the chapter 4, indium composition of InGaN/GaN MQWs is analyzed. The analysis and discussion about indium composition and its distribution by the HRTEM and HAADF-STEM are presented. In the chapter 5, strain of InGaN/GaN MQWs and

distribution of the strain is analyzed by dark-field electron holography. Finally, the results found from this thesis are summarized and concluded in the chapter 6.

Chapter 1 Introduction

1.1 GaN Based Light Emitting Diodes

1.1.1 Light Emitting Diodes

A light emitting diode (LED) is a semiconductor diode which emits light when forward biased. An LED is a device that can undergo electroluminescence which is defined as generation of light in response to the passage of an electric current through a material under an applied electric field. The electroluminescence can be excited in a various ways which is including intrinsic, avalanche, tunneling and injection processes [1]. Intrinsic electroluminescence occurs when a semiconductor subjected to an alternating electric field. The electroluminescence can be exhibit by impact ionization of the pure semiconductor lattice. Avalanche electroluminescence can occur in a PN junction or metal-semiconductor barrier. The avalanche breakdown occurs and the resulting interband transitions emit light when the bias was reversed. Tunneling electroluminescence also occurs in a PN junction or metal-semiconductor. It has been reversed biased to the point that carriers tunnel into the active material from the metal contacts and the resulting interband transitions result in emitted light. Finally, injection electroluminescence occurs is by far the most important method of excitation. When a PN junction is forward biased and the movement of minority carriers

across the junction leads to radiative recombination of carriers and the emission of light. Specifically, LEDs fall into this case of injection electroluminescence.

As described above, LED is based on a PN junction diode. This diode is composed of a p-type semiconductor material in direct junction with an n-type semiconductor material. After joining p-type and n-type semiconductor, the excess carriers will start to diffuse across the junction. The minority carriers cross the junction and recombine with the majority carriers already present, they leave ionized acceptor and donor atoms of the opposite charge. A negatively charged region is on the p-side and a positively charged region is on the n-side. This forms a “built-in” electric field across the junction. This electric field makes a drift current shich occurs in the opposite direction of the diffusion current. The thermal equilibrium is reached if these two currents balance out.

The field of light-emitting diodes (LEDs) has been evolving over the several decades. LEDs became powerful and high energy efficient, with a variety of different emission wavelengths from UV and violet [2] (AlGaN and InGaN based) to deep red (based on GaP and its ternaries) diodes, multicolor and white LEDs [3-7]. This technology has developed into solid-state lighting (SSL), next generation light sources. Therefore it is attracting huge attention from the various field.

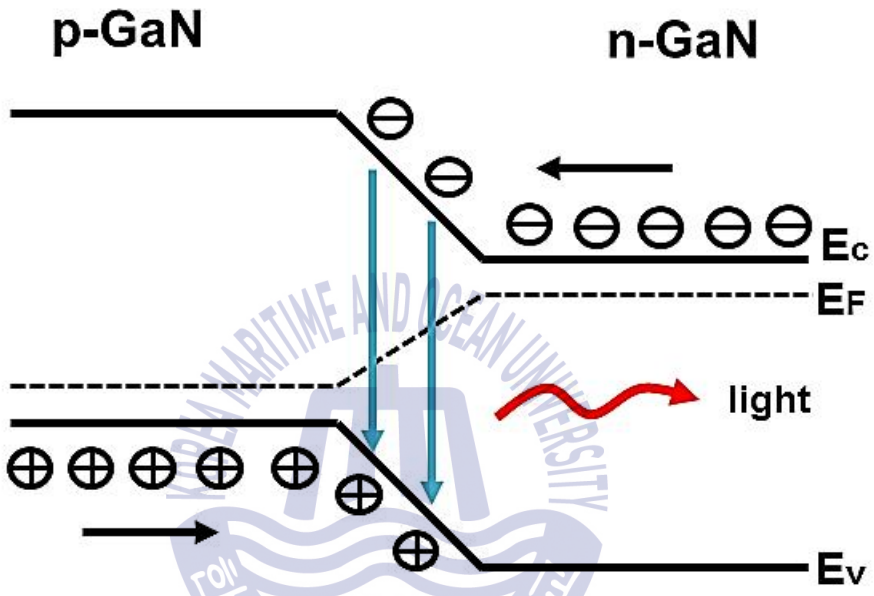

Figure 1. 1 Band Diagram of a PN Junction in the light emitting diodes

The producers wanted to improve quality of white LEDs and down its fabrication costs, in order to make LEDs more attractive for the customers.

Even if white LEDs are widely used now, both their high price and slightly worse color rendering compared to the conventional light sources should need new technology to make better and cheaper. Currently available white LEDs are based on the Ill-nitride material system with adding color conversion materials such as phosphors [7-9], allowing to mix violetblue color from InGaN and yellow color from phosphor. InGaN is very important material which can be the only available material for short wavelength emission in the visible light spectrum, however phosphor as the color conversion material can and should be optimized.

White LEDs is made by a stack of epitaxially grown InGaN quantum wells (QWs) of different indium concentration which can cover blue, green and yellow parts of the light spectrum [10]. Usually, Two more types of white LEDs, three individual red-green-blue (RGB) diodes, and stacked QWs. currently available. RGB diodes are packed in the same enclosure to make white light by mixing three colors. Stacked QW WLEDs are based on epitaxial grown QWs emitting at different wavelengths. Therefore, the development of GaN-based LEDs has been becoming a huge effect on lighting technology.

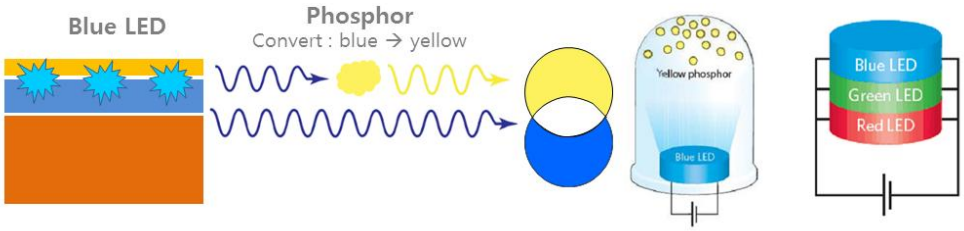

Figure 1. 2 The principle of white LED [8]

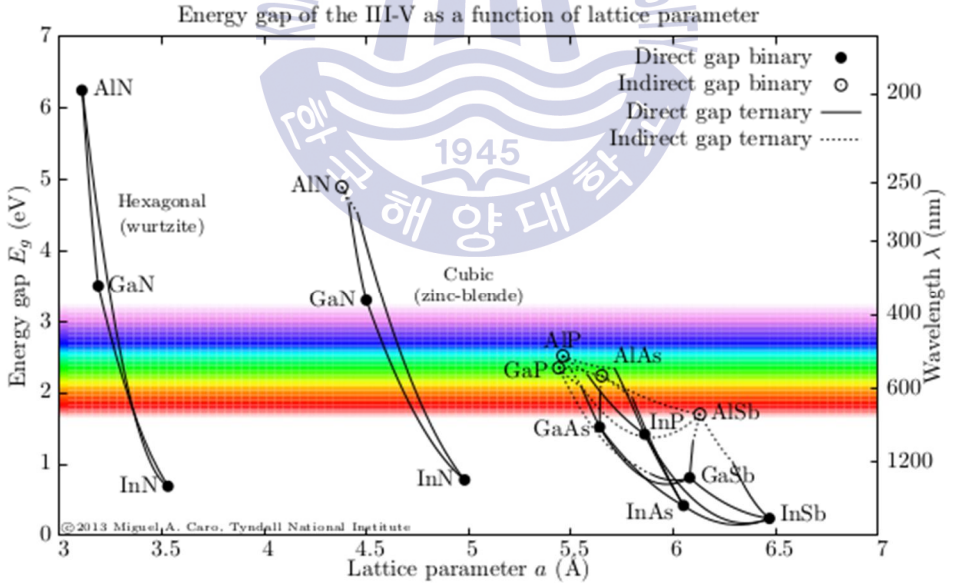

Figure 1. 3 Energy gap of the III-V as a function of lattice parameter

1.2.1 History of GaN-based LED development

The GaN-based material has been investigated since research into semiconductors as light emitters. In 1959 Grimmeiss et al. [11] employed the same technique as Johnson et al. [12] and Juza and Hahn[13] to make small crystals of GaN for measuring their photoluminescence spectra. However GaN crystal was very small. Large area layers of GaN were first produced in 1969, GaN films on sapphire were grown by chloride vapor technique[14]. The success enhanced the research and in 1971 Dingle et al. [15] demonstrated stimulated emission from optically pumped GaN. Subsequently, an electrically pumped Zn doped M-i-n (M: metal) device emitting in the blue region of the spectrum and an Mg-doped violet M-i-n structure in 1973, were demonstrated [16-17]. Although this initial progress was promising the production of p-type GaN is difficult to prove and, without the ability to produce p-n junctions in nitrides, so researchers studied other material, such as ZiSe and SiC, to produce blue/violet light emitters.

After 15 years, Amano et al. [18-19] managed to solve the problem of producing p-type GaN. They discovered that after Low-Energy Electron Beam Irradiation (LEEBI), the highly resistive Mg doped GaN had become conductive. To explain it, Van Vechten et al. [20] proposed that hydrogen formed a complex with the Mg acceptor; the energy of the LEEBI broke this bond producing a shallow Mg acceptor level. Nakamura et al. [21-22]

reported that the p-type material could also be achieved by thermal annealing at temperatures above 600°C. Nakamura produced the first high brightness (over 1 candela) InGaN/AlGaN blue LED [23]. He produced the first nitride based laser and first violet nitride laser in 1997 and in 1999 Nichia announced commercial violet laser diodes [24-25].

1.2 InGaN/GaN Multi-quantum Wells in Light Emitting Diodes

1.2.1 Multi-quantum Wells in Light Emitting Diodes

A quantum well is a particular kind of heterostructure in which one thin "well" layer is surrounded by two "barrier" layers. Both electrons and holes see lower energy in the "well" layer, hence it calls by a "potential well". This layer is so thin (about 100 Å or about 40 atomic layers) and it showed that the electron and hole are both waves. The allowed states in this structure correspond to standing waves in the direction perpendicular to the layers. Because only particular waves are standing waves, the system is quantized, hence the name "quantum well".

One-dimensional quantum wells are formed through alternating layers of semiconductor materials with different band gaps. A single quantum well is formed from one layer sandwiched between two layers which has a larger band gap. The centre layer with the smaller band gap forms the QW, while the two layers and the centre layer create the potential. Two potential wells

are actually formed in the QW structure. The well depth for electrons is the difference between the conduction-band edges of the well and barrier semiconductors, while for holes one is the corresponding valence-band offset. Multiple quantum well structures are made up a series of QWs. This type of structure is sufficient to prevent significant electronic coupling between the wells, then each well is electronically isolated. Quantum wells are thin layered structures and many quantum mechanical effects can observe and control. In the QWs show their special properties from the quantum confinement of charge carriers in thin layers of "well" material sandwiched between other semiconductor "barrier" layers. Basic properties of a quantum well can be understood through the simple "particle in a box" model. Here we consider Schrödinger's equation in one dimension for the particle of electron or hole,

$$\frac{\hbar^2}{2m}\frac{d^2\phi_n}{d_z^2} + V(z)\phi_n = E_n\phi_n \qquad (1.1)$$

where V(z) is the structural potential seen by the particle along the direction of interest (z), m is the effective mass, and En and ϕn are the Eigen energy and Eigen function associated with the n^{th} solution to the equation. The simplest case is shown in Fig. 1.4. In this "infinite well" case, it presume that the barriers on either side of the quantum well are infinitely high.

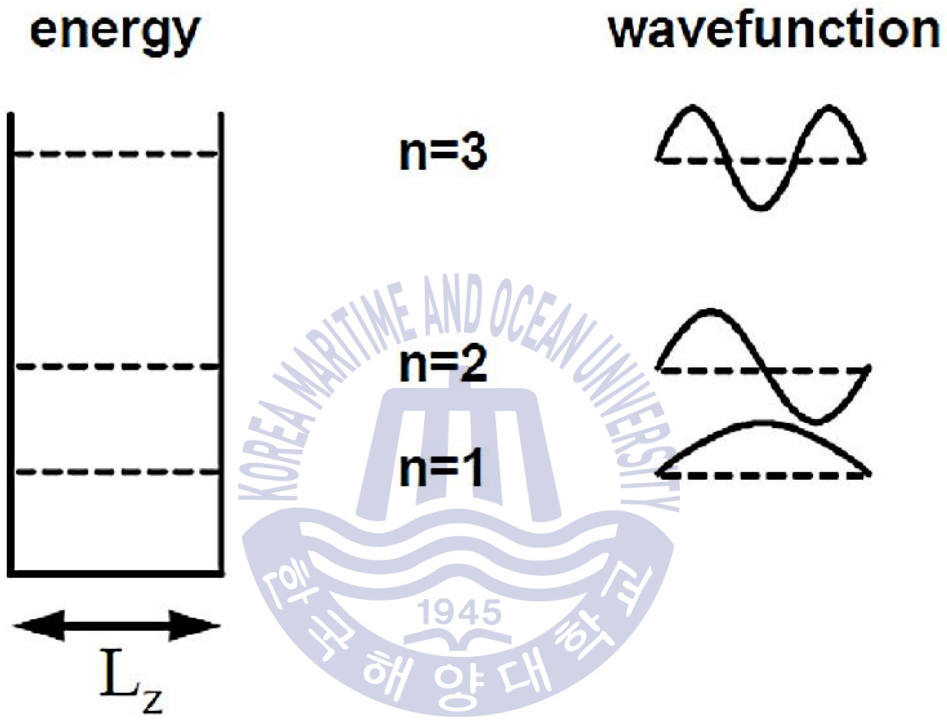

Figure 1.4 Infinite quantum well and associated wave functions.

Then the wave function must be zero at the walls. The solution is follows:

$$E_n = \frac{\pi^2\hbar^2 n^2}{2m*L_z^2} \qquad n = 1,2 \ldots\ldots \qquad \phi_n = Asin\phi(\frac{n\pi z}{L_z}). \quad (1.2)$$

The energy levels are quadratically spaced, and the wave functions are sine waves. In this formula, the energy shows to the energy of the bottom of the well. Note that the first energy is above the bottom of the well. The the first allowed electron energy level in a typical 100 Å GaAs quantum well is about 40 meV, which is close to the value calculated by this simple formula. This scale of energy can be seen even at room temperature. The solution of the problem of finite quantum well is an easy mathematical exercise. However it need considering that the wave function must be continuous.

Fig. 1.5 illustrates the differences between the "infinite" quantum well, the actual "finite" well. In contrast to bulk semiconductors, excitonic effects are very clear in quantum wells at room temperature, and which can influence on device performance. The simplest model for absorption between the valence and conduction bands in a bulk semiconductor is to shows that an electron from the valence band to a state of essentially the same momentum in the conduction band can be raise by absorbing a photon.

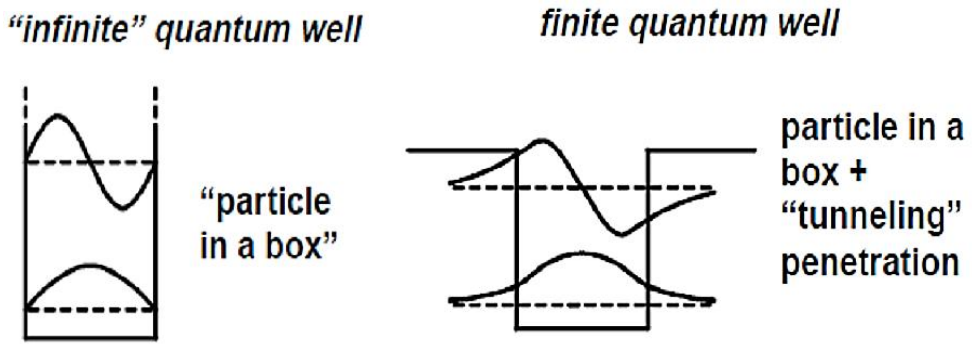

Figure 1.5 Comparison of "infinite" quantum well and "finite" quantum well behavior.

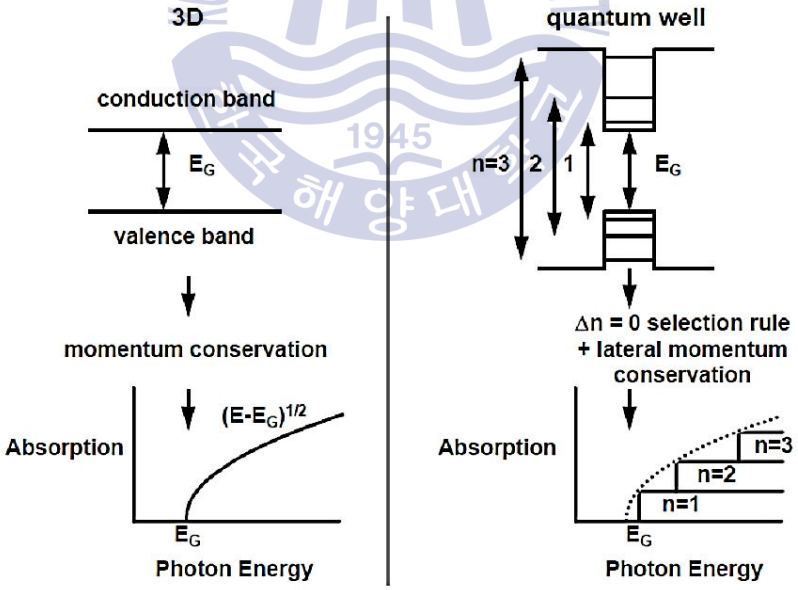

Figure 1.6 Optical absorption in bulk (i.e., 3D) semiconductors and in quantum wells

The state in the conduction band must have the same momentum because the photon has essentially no momentum in semiconductors. In this simple model, it is also presumed that all transitions have identical strength, although they will have different energies which for such vertical transitions. Therefore optical absorption spectrum has a directly from the density of states in energy, and in bulk semiconductors, the result is an absorption edge that increase as the square root of energy, as shown in Fig. 1.6.[26]. In a quantum well, the electrons and holes are still free to move in the directions parallel to the layers. Hence, "sub-bands" is present which start at the energies calculated for the confined states. The electron in a confined state can have any amount of kinetic energy for its in-plane motion, and so can have any energy larger than or equal to the simple confined-state energy for sub-band. The density of states in the plane turns out constantly with energy, so the density of states for a given sub-band is a "step" which starts at the confinement energy. Optical transitions must still conserve momentum in this direction and just as for bulk semiconductors. Hence, in this simple model, the optical absorption in a quantum well is presented as a series of steps, while one step is each quantum number, n. It can be shown easily from the known densities of states, that the corners of the steps "touch" the square root bulk absorption curve. Thus, when imagine increasing the quantum well thickness, a smooth transition to the bulk behavior will be made, with the

steps until they merge into the continuous absorption edge of the bulk material. For example, room temperature absorption spectrum of a GaAs/$Al_{0.28}Ga_{0.72}$ As MQW structure which containing 40 periods with 7.6 GaAs quantum well is shown in Fig. 1.7. The spectrum of GaAs at the same temperature is shown for comparison. From Fig. 1.7, the quantum well absorption is certainly a series of steps, and calculations based on the particle-in-a-box models will give the approximate positions of the steps. Detailed analysis reveals that the exciton binding energies of the quantum well are about 10 meV, higher than the value of 4.2 meV in bulk GaAs. The enhancement is a result of the quantum confinement of the electrons and holes in the QW. The excitons are still stable at room temperature in the QW. The bulk sample shows a weak shoulder at band edge, but the MQW shows strong peaks which from the heavy and the light hole excitons. The lifting of the degeneracy originates from the different effective masses and the lower symmetry of the QW sample. Semiconductor quantum wells are excellent case of quantum mechanics in action. The reduced dimensionality has led to major advances in the understanding of 2-D physics and the applied science of optoelectronics. The devices with QW structures show very attractive performance characteristics and impressive yields. Thus the MQWs are essential as an active region in the LED [27].

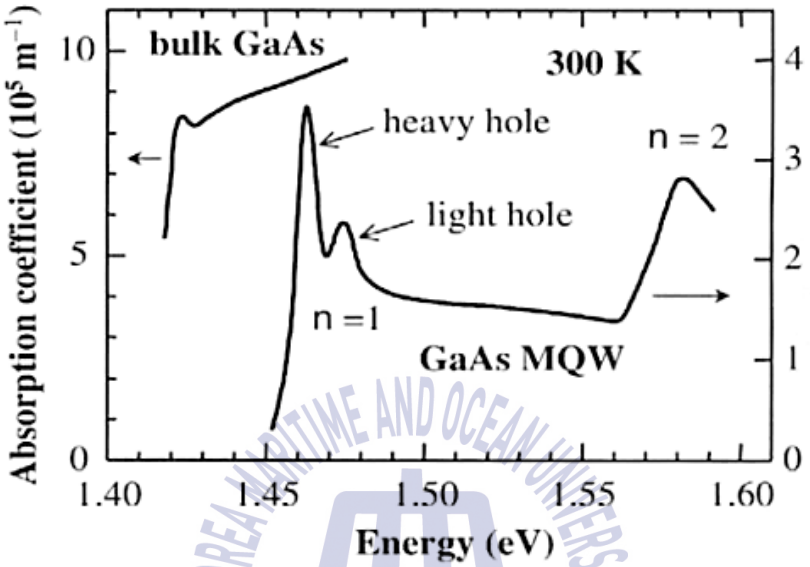

Figure 1.7 Room temperature absorption spectrum of GaAs/ $Al_{0.28}$ $Ga_{0.72}As$ MQW structure.

1.2.2 Problems in InGaN/GaN MQWs

1.2.2.1 Phase Segregation

A phase separation is a significant problem for the application of III-nitrides, which can give a unfavorable effect on the alloy electronic and optical properties. Therefore, the study of the growth and thermodynamics of the InGaN system is greatly important. The growth of high quality InGaN films is difficult, especially the indium composition is above 20%, because of phase separation. The nitride films are grown at high temperatures in order to dissociate ammonia (NH3) and free up nitrogen for bonding. However, the InN bond is significantly weaker than that for GaN at high temperatures, so InGaN films will have difficulty with indium incorporation. If the temperature is lowered, hydrogen will etch nitrogen away from the indium on the growth surface. The Indium incorporation, and an inherent miscibility gap in the InGaN alloys, can lead to compositional variations and spinodal phase separation. Also, there are large strain energies in InGaN films grown on GaN, due to the large misfit of lattice parameter between GaN and InN. But lattice misfit relaxation is obstruct by crystal geometry, where the basal slip planes lie perpendicular to the crystal growth direction. Therefore, phase separation can lead to a significant reduction of the InGaN strain energy when the strain is too high.

Phase separation in the InN–GaN alloy system occurs while a miscibility

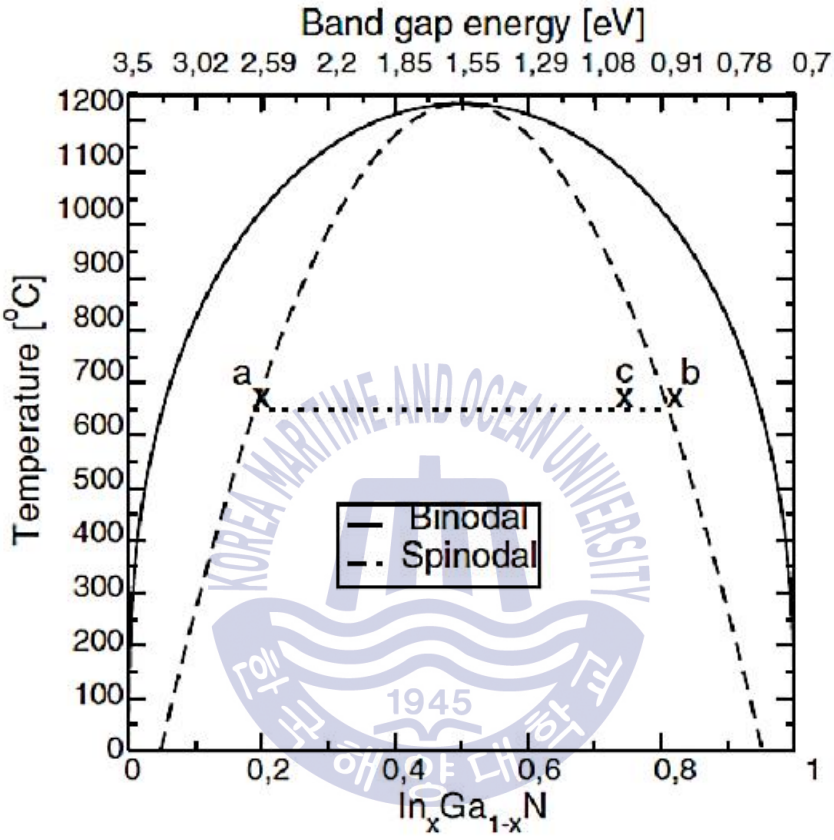

Figure 1.8 Free energy curve and the regions in the phase diagram associated with spinodal decomposition [28].

gap develops between the two binary species, InN and GaN. Fig. 1.8 shows the free energy curve for a binary system and the regions on the phase diagram. Equilibrium phase compositions are those corresponding to the free energy minima. The boundary of the unstable region is found by performing a tangent construction of the free-energy diagram. The spinodal decomposition regions have negative curvature in the corresponding free energy versus composition curve. The free energy change in the spinodal region is negative for small fluctuations in composition. Thus the system is unstable and can cause composition fluctuations. As a result phase separation will occur [28].

Tabata et al. also reported phase separation suppression in $In_xGa_{1-x}N$ alloy layers because of external biaxial strain, while the phase separation is occurred in the relaxed InGaN samples [29]. It shows that the composition pulling effect is an important in suppressing phase separation around InGaN/GaN interfaces [30-31]. The composition pulling effect limits indium incorporation around interfaces because of the existence of large strain. The lowered indium incorporation can reduce the driving force for phase separation and increases the critical thickness for relaxation. During growth process, the layer progressively relaxes, eventually forming phase separation.

Even though, many researchers have been studied about strained films of InGaN.

1.2.2.2 Indium fluctuation

Internal quantum efficiencies and properties of light emitted from the active layer depend on the variation difference of Indium layer and quantum confined Stark effect caused by the strain. Some places with higher radiative recombination by In concentration variation is called intense luminous centers [32]. Fluctuation of Indium in the active layer provides high quantum efficiency by quantum dot [33]. Internal quantum efficiency of InGaN/GaN LEDs with low indium is around 90% [34]. It also affects the polarization stage of the emitted light. As the indium concentration is increased, uniformity of In along the layer decreases, so it results in lower emission polarization. While the indium concentration is decreased, well layer becomes more homogeneous and the compressive strain starts to dominate on the emission property. And indium fluctuation is influence to polarization component. Therefore, the wavelength of InGaN can have a limit of Indium concentration, degree of optical polarization increases [35]. This fact shows that why InGaN/GaN LEDs illuminate with high power have high density of defects. Temperature is also problem for In fluctuation because of thermal instability of InGaN. The defects by metal migration may short the diode which is an issue of LEDs. Indium fluctuation in InGaN quantum well region increases internal quantum efficiency. However, higher indium composition in QW layer causes decomposition of the structure which decreases the

quantum efficiency for higher wavelengths due to the high lattice mismatch between InN and GaN. Internal quantum efficiency of 450, 520 and 540 nm LEDs are 60%, 35%, and 10% respectively [36]. Moreover, decrease of indium concentration or no indium in quantum well will also result in lower quantum efficiency and optical power output. When the indium is without in the well, no indium fluctuation forms localized energy state can take place. As a result, carriers will be trapped into high number of non-radiative recombination centers. Therefore, as the Indium concentration becomes to zero, internal quantum efficiency decreases.

1.2.2.3 Defects

The dislocation, which is extended defect, play the central role in the development of nitride material and device technology. Due to the lack of GaN substrates, the GaN layer is grown on heterogeneous substrate such as c-plane sapphire, hexagonal SiC or Si (111), etc. However, the heteroepitaxy of nitrides suffers from a large lattice and thermal expansion coefficient mismatch. The growth of thick structures includes dislocations, strain and strain-induced cracking. During the nucleation of the first nitride layer, a high dislocation density is formed and they tend to thread upwards. The high dislocation density decreases the efficiency of the optical and electrical performance of devices. To reduce the dislocation density in the active

region, intermediate layers are used, such as, AlN/AlGaN superlattice [37] or employed epitaxial lateral overgrowth. Nevertheless, even in a good quality ternary nitride layer has the high dislocation density about 10^8 to $10^9 cm^{-2}$. The extended defects provide detrimental effect to the device. They can accumulate point defects, and serve as efficient nonradiative recombination centers [38]. And they may serve as high conductivity channels, for example, LEDs transporting injected carriers through the structure without recombination. In some cases of InGaN QWs, dislocations seem to be surrounded by potential barriers, which prevent carrier capture and the subsequent nonradiative recombination. On the contrary, in the case of AlInN, strong strain-induced alloy composition fluctuations have been found, which should lead to an efficient nonradiative recombination [39]. There are many researches, however, the effect of dislocations to the carrier recombination in nitrides is still under debate. InGaN QW LEDs shows very high efficiency even for dislocation densities of the order of $10^9 cm^{-2}$. While GaAs or InP-based devices have dislocation densities 4 to 5 orders smaller than that.

1.3 Purpose and Contents of This Study

The problems of InGaN/GaN MQWs have been researched and the efficiency of LED was developed. However, analysis was carried out by existing methods which are difficult to analyzed MQWs with thin and

complex structures. Therefore we think that TEM techniques are essential for MQWs to analyze in the atomic scale with their high resolution.

In this thesis, indium composition and strain were quantitatively analyzed by HRTEM, HAADF-STEM and DFEH techniques.

The contents of this thesis are divided as the following chapters:

Chapter 2: The detailed experimental procedure in this study will be presented.

Chapter 3: The microstructural details of the GaN film grown on a cone-shaped patterned Al_2O_3 substrate were investigated using high-resolution transmission electron microscopy (HRTEM) and weak beam dark-field techniques. Various defects such as misfit dislocations (MDs), recrystallized GaN (R-GaN) islands and nano-voids were observed by HRTEM. And the distribution of dislocation will be investigated by weak beam dark-field techniques.

Chapter 4: Quantitative analysis of indium composition by the HRTEM and high angle annular scanning TEM (HAADF-STEM) will be presented. The indium compositions obtained by lattice constant from HRTEM images will

be compared with the high-resolution X-ray diffraction data. And the relative indium composition will be obtained from intensity of HAADF-STEM image.

Chapter 5: Strain analysis of InGaN/GaN MQWs by dark-field electron holography (DFEH) will be presented. The strain mapping image will be obtained from DFEH image of InGaN/GaN MQWs. And the strain distribution will be investigated.

Chapter 6: The main results of the present work will be summarized.

REFERENCES

[1] S.M Sze. and K.K Ng: *Physics of Semiconductor Devices*, 3rd Edition (2006).

[2] T. Nishida, H. Saito, and N. Kobayashi, *Appl. Phys. Lett*. **79**, 711 (2001).

[3] H. P. Xin, R. J. Welty, and C. W. Tu, *Appl. Phys. Lett*. **77**, 1946 (2000).

[4] M. R. Krames, M. Ochiai-Holcomb, G. E. Höfler, C. Carter-Coman, E. I. Chen, I.-H. Tan, P. Grillot, N. F. Gardner, H. C. Chui, J.-W. Huang, S. A. Stockman, F. A. Kish, M. G. Craford, T. S. Tan, C. P. Kocot, M. Hueschen, J. Posselt, B. Loh, G. Sasser and D. Collinset, *Appl. Phys. Lett.,* **75,** 2365 (1999).

[5] F. A. Kish, F. M. Steranka, D. C. DeFevere, D. A. Vanderwater, K. G. Park, C. P. Kuo, T. D. Osentowski, M. J. Peanasky, J. G. Yu, R. M. Fletcher, D. A. Steigerwald, M. G. Craford and V. M. Robbins. *Appl. Phys. Lett*. **64** 2839 (1994).

[6] M. J. Grundmann' and U. K. Mishra, *Phys. Sta. Sol. (c)* **4**, 2830 (2007)

[7] Y. Narukawa, I. Niki, K. Izuno, M. Yamada, Y. Murazak and T. Mukai, *Jpn. J. Appl. Phys*. **41**, L371 (2002).

[8] S. Pimputkar, J. S. Speck, S. P. DenBaars, and Shuji Nakamura. *Nature Photonics* **3**,180 (2009).

[9] P. Yang, X. Yua, X. Xu, T. Jiang, H. Yu, D. Zhou, Z. Yang, Z. Song, J. Qiu, *J. Sol. Stat. Chem*. **202**, 143 (2013).

[10] W. Guo, M. Zhang, A. Banerjee, and P. Bhattacharya, *Nano letters*, **10**, 3355 (2010).

[11]H. Grimmeiss and Z. H-Koelmans, *Nature*, **14**, 264 (1959).

[12] W. C. Johnson, J. B. Parsons, and M. C. Crew, *Journal of Physical Chemistry*, **234**, 2651(1932).

[13]R. Juza and E. Hahn, *Anorg. Allgem. Chem*., **234**, 282 (1938) .

[14]H. P. Maruska and J. J. Tietjen, *Appl. Phys. Lett*., **15**, 367 (1969)

[15] R. Dingle, K. L. Shaklee, R. F. Leheny, and R. B. Zetterstrom, *Appl. Phys. Lett*., **19** , 5 (1971)

[16] J. I. Pankove and E.A. Miller. *Journal of Luminescence*, **5**, 84 (1972).

[17] H.P. Maruska, D. A. Steveson, and J. I. Pankove, *Appl. Phys. Lett.,* **22,** 303 (1973).

[18] H. Amano, I. Akasaki, T. Kozawa, K. Hiramatsu, N. Sawaki, K. Ikeda., *Journal of Luminescence*, **40,** 121 (1988).

[19] H. Amano, M. Kito, K. Hiramatsu, and I. Akasaki. *Jpn. J. Appl. Phys***.** **28**, L.2112 (1989) .

[20] J, A. Van Vechten, J. D. Zook, R. D. Horning and B. Goldenberg., Japanese Journal of Applied Physics 31 (1992) 3662

[21] S. Nakamura, T. Mukai, M. Senoh, and N, Iwasa, *Jpn. J. Appl. Phys*, **31**, L139 (1992).

[22] S. Nakamura, N. Iwasa, M. Senoh, and T. Mukai. *Jpn. J. Appl. Phys,* **31,** 1258 (1992).

[23] S. Nakamura, T. Mukai, and M. Senoh,. *Appl. Phys. Lett*., **64** , 1687 (1994).

[24] S. Nakamura, *Mater. Sci. Eng. B* **43**, 258 (1997).

[25] S. Nakamura, *Journal of Crystal Growth*, **170**, 11 (1997)..

[26] S. Gasiorowicz: *Quantum Physics*, 2nd edn. (Wiley, New York 1996)

[27] D. A. B. Miller, D. S. Chemla, D. J. Eilenberger, P. W. Smith, A. C. Gossard, and W. T. Tsang,. *Appl. Phys. Lett*. **41**, 679 (1982).

[28] I. Ho and G. B. Stringfellow, *Appl. Phys.Lett*. **69,** 2701 (1996).

[29] A. Tabata, L. K. Teles, L. M. R. Scolfaro, J. R. Leite, A. Kharchenko, T. Frey, D. J. As, D. Schikora, K. Lischka, J. Furthmüller and F. Bechstedt, *Appl. Phys. Lett*. **80**, 769 (2002).

[30] M. Rao, D. Kim, and S. Mahajan, *Appl. Phys. Lett.* **85**, 1961 (2004).

[31] K. Hiramatsu, Y. Kawaguchi, M. Shimizu, N. Sawaki, T. Zheleva, R. F. Davis, H. Tsuda, W. Taki, N. Kuwano, and K. Oki, *MRS Internet J. Nitride Semicond. Res*. **2**, 6 (1997).

[32] J. Ruan, T. J. Yu, C. Y. Jia, R. C. Tao, Z. G. Wang, and G. Y. Zhang, *Chin. Phys. Lett*., **26**, 037902 (2009).

[33] T. A. Truong, L. M. Campos, E. Matioli, I. Meinel, C. J. Hawker, C. Weisbuch, and P. M. Petroff , *Appl. Phys. Lett*., **94**, 023101 (2009).

[34] Lu Chen and Arto V. Nurmikkov, *Appl. Phys. Lett*., **85**, 3663 (2004) .

[35] C. H. Chiu, S. Y. Kuo, M. H. Lo, C. C. Ke, T. C. Wang, Y. T. Lee, H. C. Kuo, T. C. Lu, and S. C. Wang, *Journal of Applied Physics* **105**, 063105 (2009)

[36] J.-H. Ryou, P. D. Yoder, J. Liu, Z. Lochner, H. Kim, S. Choi, H. J. Kim,

and R. D. Dupuis, *IEEE journal of selected topics in quantum electronics*, **15,** 1080 (2009).

[37] M. S. Shur and R. Gaska, *Proc. SPIE* **6894**, 689419 (2008).

[38] A. Pinos, S. Marcinkevičius, M. Usman, and A Hallén, *Appl. Phys. Lett.* **95**, 112108 (2009).

[39] F. Hitzel, G. Klewer, S. Lahmann, U. Rossow, and A. Hangleiter, *Phys. Rev. B* **72**, 081309 (2005).

Chapter 2 Experiments

2.1 Structures of samples

We prepared thin InGaN layers with different In compositions. Test samples A (T-A) and B (T-B) were grown on thick GaN films on a sapphire (0001) substrate by metal organic chemical vapor deposition. The thicknesses of the InGaN layers in T-A and T-B, as determined from TEM, were ~35.4 and ~37.8 nm, respectively.

And the samples used in this work were extracted from a commercial LED chip as shown in Figure 2.1. The MQWs were positioned between a 7-μm-thick Si-doped GaN layer on the patterned sapphire substrate and a 200-nm-thick Mg-doped GaN capping layer. The InGaN/GaN MQWs contained three 2-nm-thick InGaN wells with 6-nm-thick GaN barriers (Low-In region) and five 3-nm-thick InGaN wells with 2-nm-thick GaN barriers (High-In region).

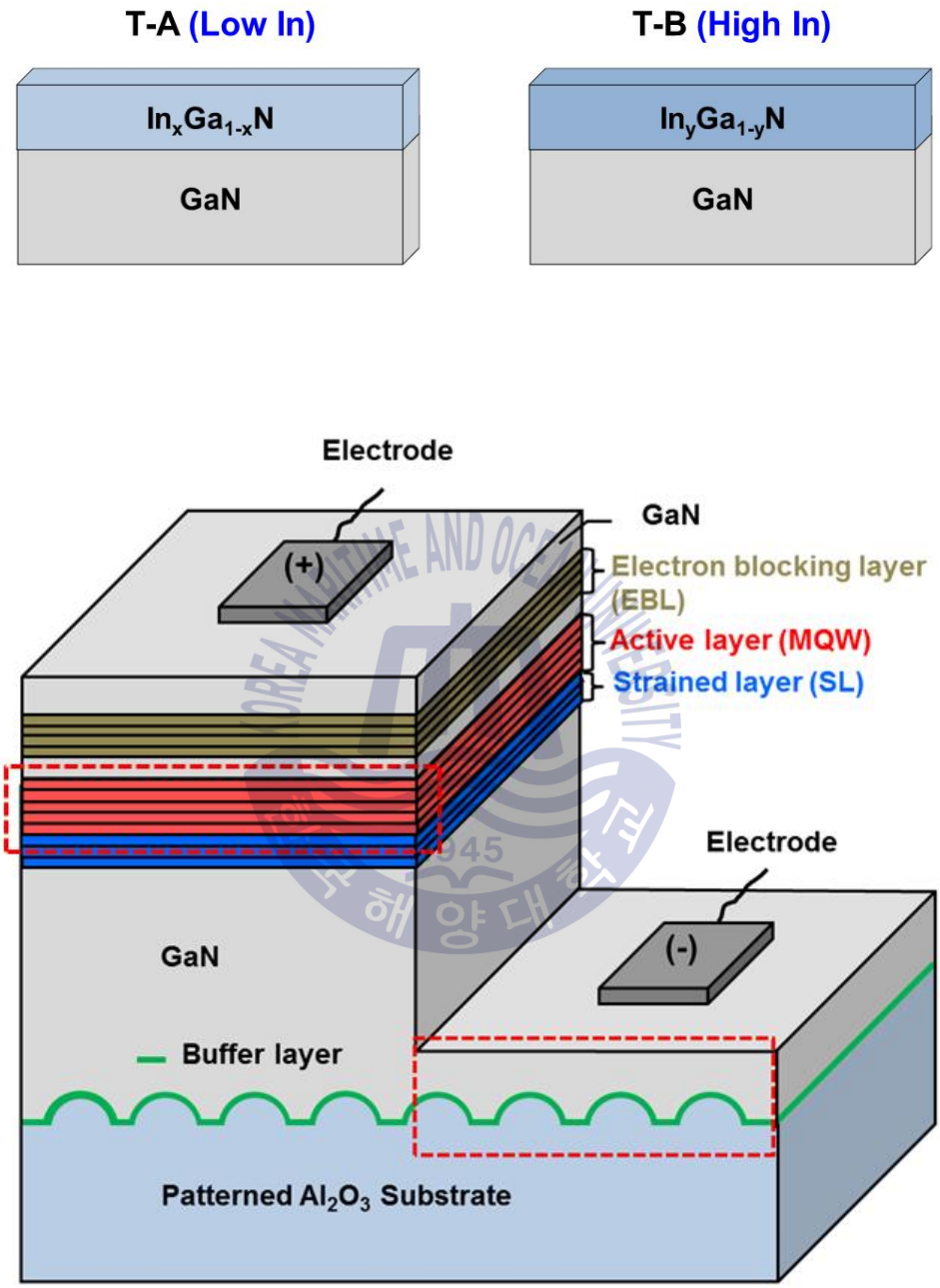

Figure 2.1 schematic image the structure of single layers and LED.

2.2 Rutherford Backscattering Spectroscopy

Rutherford backscattering spectrometry (RBS), as a technique to address thin film properties in materials research, has evolved from classical nuclear physics experiments conducted during the first half of the previous century. In the 1960's it was developed to a standard analysis technique particularly useful for the growing semiconductor field. The basic principle is contained in the kinematics for binary collisions. A beam of known particles (ions) with mass M1 is given the energy E0 and directed onto the sample containing the particles M2 that are to be investigated (Figure 2.2).

The energy E1 and the scattering angle Θ of the particle M1 are detected. From the conservation laws of energy and momentum, it is then possible to deduce the mass of the target particles M2. Furthermore, since the probability of scattering in a certain angle is known by the so called Rutherford cross section, it is also possible to estimate the abundance of M2 particles in the sample by counting the yield of scattered particles M1 in a certain solid angle covered by the detector.

A typical Rutherford backscattering setup consists of a particle accelerator that can deliver beams of low-mass ions in the MeV range. A tandem accelerator is used. This machine produces negative ions that are accelerated towards positive potential. The particles are transported in a vacuum system and at the high voltage terminal electrons are stripped off

and the particle charge becomes positive. Then they are repelled by the high positive voltage and increase their energy further. The beam is then analyzed and directed to the target chamber. The beam diameter is about a millimeter at the target.

The detector, a surface barrier detector, is normally mounted in a backscattering angle Θ of, for instance, 170° from the incident beam. As the incident particles penetrate the target matrix some of them will experience the Coulomb force from target nuclei and be deflected from their path. These collisions are governed by the Rutherford cross section and a small –but sufficient- number of the deflected ions will be backscattered into the detector [1].

2.3 X-ray Diffraction

The German physicist Wilhelm Conrad Röntgen discovered X-rays in 1895. It is a high-energy electromagnetic radiation having a wavelength from about 0.001 to 10 nm. However, X-rays used to study the structure of the materials have a narrow range of wavelengths of 0.05 to 0.25 nm. For the production of X-rays, electrons are generated by heating a cathode (e.g., tungsten filament) in a vacuum chamber. These electrons are accelerated towards an anode (e.g., copper) and collide with it at a very high velocity. If the incident electron possesses sufficient energy to eject an inner-shell

electron (having lower average energy than that of outer-shell) from the atom of the anode metal, the atom will be left in the excited stage. This inner-shell is filled by an electron from an outer-shell of the atom and an X-ray photon is emitted as the atom returns to the ground state. When an experimental set up is made such a way that the monochromatic X-ray beam hits a sample, it generates scattered X-rays with the same wavelength as the incident beam. The atomic arrangement of the sample is responsible for the intensities and spatial distribution of the scattered X-rays. If the scattered waves are in phase, there is a constructive interference which forms a spatial diffraction pattern in a specific direction. These directions are governed by the wavelength (λ) of the incident beam and the structure of the sample.

The diffraction of X-rays is described by the Bragg's law which was formulated by W. H. Bragg and W. L. Bragg in 1913 [2].

$$n\lambda = 2dsin\theta \qquad (2.1)$$

Where d is the distance between each adjacent crystal planes (d-spacing), θ is the angle between the incident beam and the particular planes under consideration, also known as Bragg angle. A diffracted peak can be observed when the condition given by the Bragg's law is satisfied.

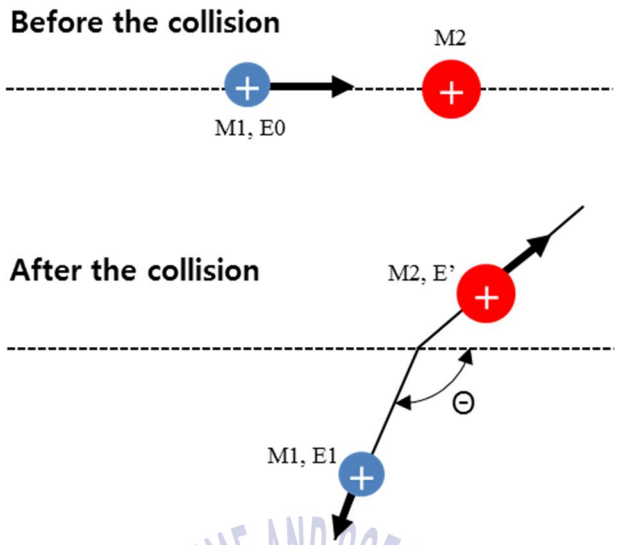

Figure 2.2 A collision between two –positivley charged- particles before and after the collision. Momentum and energy is conserved.

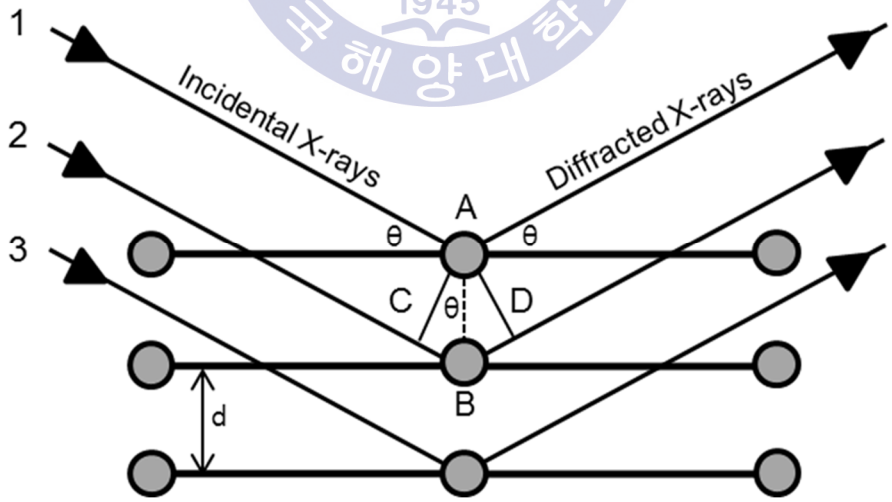

Figure 2.3 Derivation of Bragg's law showing the diffraction of X-rays.

As shown in the figure, the top X-ray beam 1, which is in-phase with the beams 2 and 3, is scattered by the atom A when it hits the top layer of the sample. On the other hand, the beam 2 goes deeper until it strikes the atom B and scattered as well. The second beam travels extra distance (known as path difference) of CB+BD which is equal to $2d\sin\theta$ if the beams 1 and 2 are to continue to travel parallel in the same direction. Now the criterion for the existence of the diffracted wave is that the scattered X-rays should all be in phase. For this, the path difference CB+BD must be equal to an integral number (n) of the wavelength (λ) of the incident beam. This is the Bragg‟s law. The angle between the incidental beam and the diffracted beam is 2θ which is usually measured during the experiment. Depending on the lattice planes of the crystal structure, diffracted X-rays produce constructive interference at a certain Bragg angle. Different crystal planes in a lattice can be described by Miller indices which are represented by three integers (hkl). These indices are important for the interpretation of X-ray diffraction pattern. X-ray diffraction peaks can be used to determine the size of small crystallite in the sample. The expression is known as Scherrer Equation which is given by

$$L = \frac{k\lambda}{B\cos\theta}. \qquad (2.2)$$

Where L is the average crystallite size measured in a direction

perpendicular to the surface of the specimen, λ is the wavelength of the X-ray used, B is the full width at half maximum (FWHM) of the characteristic crystalline peak, θ is the Bragg angle and k is the Scherrer constant. K has been determined to vary between 0.89 and 1.39, but is usually taken as close to unity [3]

2.4 Transmission Electron Microscopy

The wave-like characteristics of electrons were first postulated in 1925 by Louisde Broglie, with a wavelength far less than visible light. In 1926 H. Busch revealed that an electromagnetic field might act as a focusing lens on electrons. The first electron microscope was constructed in 1932 by Ernst Ruska. For his research, he was awarded in 1986 the Nobel price together with Binnig and Rohrer who invented the scanning tunneling microscope. The Electron microscope opened new horizons to visualize materials structures far below the resolution reached in light microscopy. The most attractive point is that the wavelength of electrons is much smaller than atoms and it is at least theoretically possible to see details well below the atomic level. However, currently it is impossible to build transmission electron microscopes with a resolution limited by the electron wavelength, mainly because of imperfections of the magnetic lens. In the middle of the 70's the last century commercial TEMs became available that were capable

of resolving individual columns of atoms in crystalline materials. High voltage electron microscopes, i.e. with accelerating voltages between 1 MV and 3 MV have the advantage of shorter wavelength of the electrons, but also radiation damage increases. After that period HRTEMs operating with intermediate voltages between 200 kV – 400 kV were designed offering very high resolution close to that achieved previously at 1MV. More recently, developments were seen to reconstruct the exit wave (from a defocus series) and to improve the directly interpretable resolution to the information limit. New developments for increasing the resolution in high-resolution electron microscopy are the use of a monochromator and an Cs corrector to reach resolutions below 0.1 nm [4]

In this study, two different transmission electron microscopes were used, a JEM ARM-200F microscopy operated at 200 kV and a JEM-3011 operated at 300 kV. And used TEM techniques will be explained in each chapter.

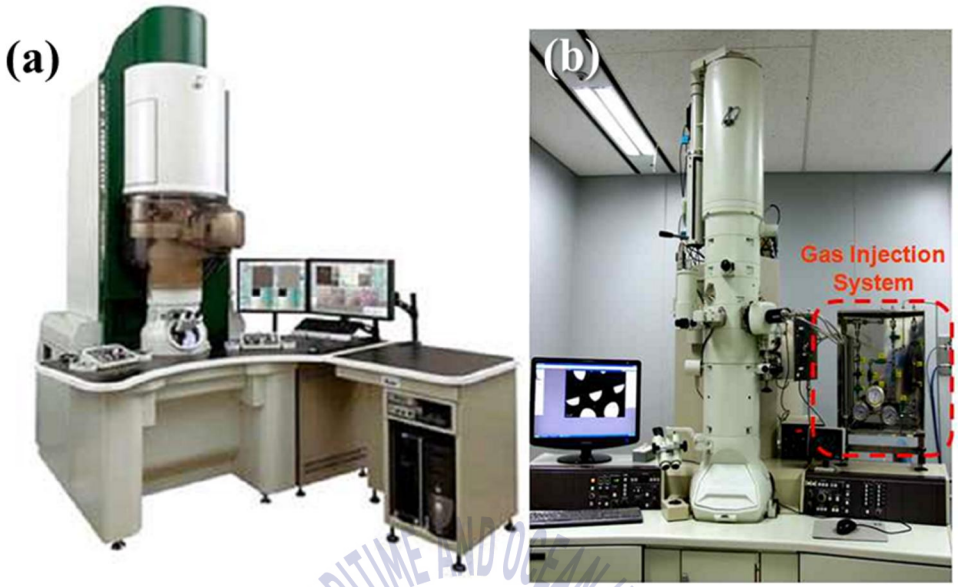

Figure 2.4 (a) JEM-ARM200F (200kV) (b) JEM-3011 (300kV)

Figure 2.5 The electron microscope built by Ruska (in the lab coat) and Knoll, in Berlin in the early 1930s.

2.5 Specimen Preparation for Transmission Electron Microscopy

In order to investigate the microstructure of materials by using transmission electron microscopes, specimens must be very thin for transmitting and scattering of incident electrons. Thus a number of ultra-thinning techniques have been developed for the preparation of TEM specimens, e.g., electropolishing, chemical polishing, ion milling, ultra-microtomy, crashing, replica and so on. Among them, ultra-microtomy has been mainly applied to organic materials. However, under the oprimum slicing conditions, satisfactory thin sections for TEM observation were successfully obtained in advanced ceramic materials, e.g., hematite (α-Fe_2O_3) particles and cadmium sulfide particles. In addition to the technique of ultra-microtomy, the focused ion beam (FIB) method of another specimen preparation technique was recently developed. The focused ion beam method technique is especially useful to investigate boundaries and interfaces by TEM.

In this study, in order to prepare TEM specimens of InGaN/GaN MQWs, FIB method was employed.

When preparing TEM specimens, the FIB essentially have to be think as an SEM with a built-in ion mill. The single ion gun produces a well-controlled beam of Ga ions (rather than Ar used in the ion mill). In the simplest design the ion beam also acts as the electron beam of the SEM with

the secondary electrons being used to form the 'SEM' image of the sample. A schematic of the FIB is given in Figure 2.6. The various stages in the preparation process are shown in Figure 2.7. The pad in (A) is the coating of Pt. The two Xs, to mark the region of interest, have been drawn on the sample using the ion beam, and another Pt strap is deposited between them (B). Next, two staircases are cut out on either side to leave the thin wall shown in (C) and (D). In (E) the 'wall' has been trimmed away at the sides so that it is only supported at the top. The last step is deposited between them (B). Next, two staircases are cut out on either side to leave the thin wall shown in (C) and (D). In (E) the 'wall' has been trimmed away at the sides so that it is only supported at the top. The last step (F) is to ion-polish the thin wall until it is really a thin TEM specimen and finally attach it to a probe for lift out or use static electricity to lift it out and place it on a supporting (usually C) film. Attaching the FIBbed specimen to a probe is becoming the norm since it allows the FIBbed specimen to be further cleaned to remove Ga contamination and/or reduce the thickness further [4]

r.

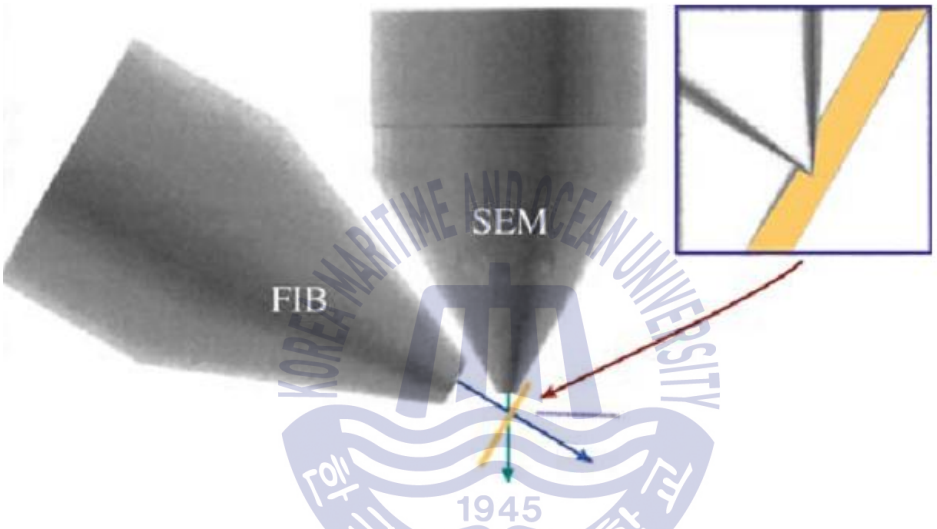

Figure 2.6 Schematic of a two-beam (electron and ion) FIB instrument

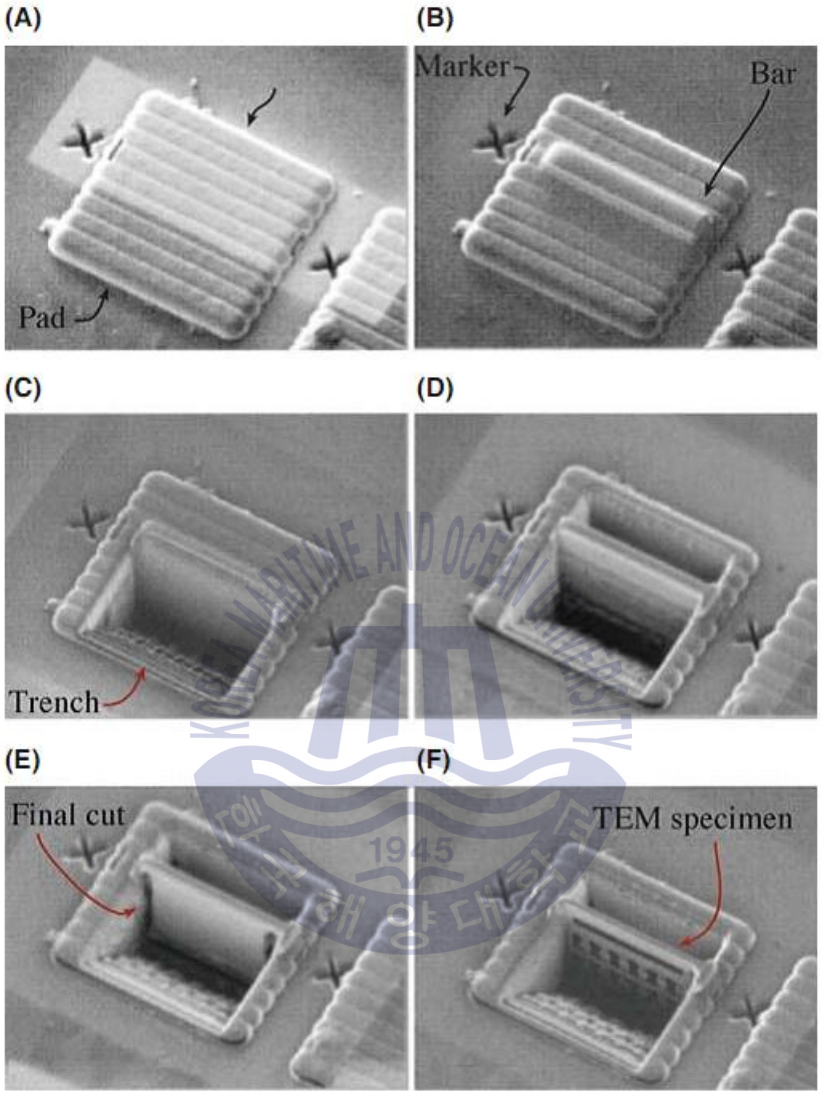

Figure 2.7 Stages in making TEMsamples using a FIB instrument. (A) The area of interest has been marked. (B) A Pt bar is deposited to protect this area from the Ga beam. (C, D) The two trenches are cut. (E) The bottom and sides of the slice are (final) cut. (F) The TEM specimen is polished in place before extracting it.

REFERENCES

[1] W. -K. Chu, J. W. Mayer, and M. -A. Nicolet: *Backscattering Spectrometry Academic Press*, New York, 1978.

[2] W. L. Bragg, *Proceedings of the Cambridge Philosophical Society* **17**, 43 (1913).

[3] A. L. Patterson, *Phys. Rev*. **56**, 978 (1939).

[4] D. B. Williams and C. B. Carter: *Transmission Electron Microscopy*, Springer, 2nd Edition, (2009).

Chapter 3 Observation of Microstructure of Light Emitting Diodes

3.1 Introduction

The field of light-emitting diode (LED) devices has been developments in since the 1960s. The high performance of GaN-based LEDs was focuced by its semi-permanent lifetime and high energy efficiency [1-2]. However, GaN-based LEDs still show relatively low internal quantum efficiency (IQE) because it has the high threading dislocation (TD) density due to the large lattice mismatch and the thermal expansion coefficients between GaN and heterogeneous substrate such as Al_2O_3 or SiC [3]. Generally, GaN-based LED chips are fabricated by the deposition of GaN on Al_2O_3 or SiC substrates using metal-organic chemical-vapor-deposition (MOCVD) [4]. After fabrication, the LED chip has various defects especially the high threading dislocation (TD) density due to the large mismatches of lattice constant and the thermal expansion coefficients between GaN and Al_2O_3 [3]. Using patterning substrate is one of the most promising method to reduce the TD density and improve the optical properties of the GaN film [5–7]. However, there is lack of detail analysis of interface and dislocation states though many researchers studied about this method. The objective of this chapter is to investigate the microstructural properties and dislocation characteristics of the GaN film grown on the embossed (cone-shape) Al_2O_3

substrate. High-resolution transmission electron microscopy (HRTEM) and weak-beam dark field (WBDF) techniques were used to observe the microstructures between the GaN film and the Al_2O_3 substrate along with the location of the cone-shaped pattern as well as to determine dislocation types and density in the GaN film.

3.2 Background of Analysis of Microstructure and Defects in GaN based Light Emitting Diodes

3.2.1 High-resolution Electron Microscopy

The fundamental idea of high-resolution transmission microscopy (HRTEM) is using both the transmitted electron wave and several diffracted electron waves when the image is formed. It increases the resolution of the image. The electron waves interfere with one another because of phase differences, an interference pattern is formed in the image plane of the objective lens. Therefore HRTEM is therefore a type of phase-contrast microscopy.

Electron scattering must be treated quantum mechanically. Actually, a 200 keV electron has a speed of approximately 0.7c (c : the speed of light in vacuum), and should be treated using quantum mechanics. [8] So it led to small spherical aberration and can achieve a high spatial resolution.

3.2.1.1 The Fourier Transform

The Fourier transform is very important to obtain HRTEM image. It is a convenient tool for analyzing images, but it especially plays a fundamental role in HRTEM theory [8]. The Fourier transform of a function f(r) is then defined as

$$F(\boldsymbol{g}) = \mathcal{F}[f(\boldsymbol{r})] \equiv \int_{-\infty}^{\infty} f(\boldsymbol{r}) e^{2\pi i \boldsymbol{g}\cdot\boldsymbol{r}}\, d\boldsymbol{r}, \qquad (3.1)$$

where r is a three-dimensional position vector in direct space and g is a three-dimensional position vector in Fourier transform, or reciprocal, space.

The inverse Fourier transform is defined as [8]

$$f(\boldsymbol{r}) = \mathcal{F}^{-1}[F(\boldsymbol{g})] \equiv \int_{-\infty}^{\infty} F(\boldsymbol{r}) e^{-2\pi i \boldsymbol{g}\cdot\boldsymbol{r}}\, d\boldsymbol{g}. \qquad (3.2)$$

When Fourier transforming a set of sampled data, the discrete Fourier transform (DFT) must be used. The most common performance of the DFT on computers is the fast Fourier transform (FFT) algorithm [8].

The two functions, f(r) and h(r), is defined as

$$f(\boldsymbol{r}) \otimes h(\boldsymbol{r}) = \int f(\boldsymbol{R}) h(r - \boldsymbol{R}) d\boldsymbol{R}. \qquad (3.3)$$

There is relating the convolution in direct space to multiplication in Fourier transform space called the convolution theorem [8]:

$$\mathcal{F}[f(\boldsymbol{r}) \otimes h(\boldsymbol{r})] = F(\boldsymbol{g})H(\boldsymbol{g}) \qquad (3.4)$$

The multiplication theorem relates multiplication in direct space to convolution in Fourier transform space [8]:

$$\mathcal{F}[f(\boldsymbol{r}) \otimes h(\boldsymbol{r})] = F(\boldsymbol{g}) \otimes H(\boldsymbol{g}) \qquad (3.5)$$

3.2.1.2 Kinematical Scattering

In quantum scattering, the wave equation is converted to integral form which can be expanded into the Born series. It can be equivalent to assuming the electron is scattered no more than once when passing through the specimen. This is called kinematical, scattering. The first Born approximation is comparable to the Fraunhofer diffraction approximation, which assumed the diffracting object to be much smaller than the distances to the source and the point of observation [9]. From the expression can derive the phase-object approximation (POA).

The POA gives the specimen transmission function, $q_e(r)$, as

$$q_e(\boldsymbol{r}) = e^{-i\sigma\varphi_p(\boldsymbol{r})}, \qquad (3.6)$$

where σ is the interaction constant and $\phi_p(r)$ is the projection of the electrostatic potential of the specimen, $\phi(r)$, along the direction of the electron beam. The interaction constant is defined as

$$\sigma = \frac{2\pi me\lambda}{h^2} \qquad (3.7)$$

where m, e, λ and h are the relativistic mass of the electron, the elementary charge, the electron wavelength and Planck's constant, respectively. If the incident wave is $\psi_0(r)$ and the exit-surface wave is $\psi_{ex}(r)$, the $\psi_{ex}(r) = q_e(r)$ $\psi_0(r)$ in the POA. Since $\psi_0(r)$ is assumed to be constant, then, $\psi_{ex}(r) = q_e(r)$.

If $\sigma\phi_p(r)$ is much less than unity, then using the first-degree Taylor polynomial of $q_e(r)$:

$$q_e(\boldsymbol{r}) \approx 1 - i\sigma\varphi_p(\boldsymbol{r}). \qquad (3.8)$$

This is called the weak phase-object approximation (WPOA). The assumption that $\sigma\phi_p(r)$ is small holds for many thin specimens [10]. For specimens are too thick for the WPOA [11]. The diffraction of electron waves by a crystal can be understood about Bragg's law. The electron waves diffracted with Miller indices *hkl* will add. Therefore,

$$2d_{hkl}sin\theta = n\lambda, \qquad (3.9)$$

where *dhkl* is the lattice-plane spacing of (*hkl*), θ is the angle between the incident wave vector and the lattice plane. A parallel lattice plane can be described by a three-dimensional reciprocal-space vector $g_{hkl} = h\boldsymbol{a}* + k\boldsymbol{b}* + l\boldsymbol{c}*$, where $|g_{hkl}| = 1/d_{hkl}$. a∗, b∗ and c∗ are the basis vectors of reciprocal space.

3.2.1.3 Dynamical Scattering

When the specimen is so thick that electron waves are scattered more than once, scattering are must considered due to the kinematical approximation, or dynamical. The dynamical effects depends on the magnitude of $\phi(r)$. When the crystal is perfectly aligned to a zone axis, $\phi(r)$ will change from a relatively large value at the atomic. The atomic columns appear as lines instead of points, when the crystal is tilted slightly from the zone axis. So the dynamical effects can be reduced since the variations in $\phi(r)$ are smaller.

Dynamical scattering causes the presence of a kinematically extinct reflection $h_3k_3l_3$ that is the result of diffraction by two or more sets of planes. In the case of double diffraction, the wave is first diffracted by the planes $(h_1k_1l_1)$ and the planes $(h_2k_2l_2)$ according to the following equations [12]:

$$\begin{aligned} h_3 &= h_1 + h_2, \\ k_3 &= k_1 + k_2, \\ l_3 &= l_1 + l_2. \end{aligned} \qquad (3.10)$$

3.2.2 Weak Beam Dark Field Image

The scattering angle in the diffraction is very small (~1 mrad). It all takes place in a narrow column parallel to the incoming electron beam. The

diffraction in the column is independent in neighboring columns. All the columns in a perfect crystal will diffract and obtain no contrast with the final image. When the crystal is not perfect, local variations in s=s(x,y,z) will be present. The amplitude of a diffracted wave for the column at (x,y) is:

$$A_g(x,y) = F_g \int_0^t e^{2\pi i s(x,y,z)z}\, dz. \qquad (3.11)$$

Using this column approximation can be derived for the case of only one strong diffracting beam (*s* is much larger or smaller than zero for all other g vectors). These Howie-Whelan equations [13] describe the change in amplitude of the direct beam φ_0 and the amplitude of the diffracted beam φ_g considering dynamical effects arising from multiple diffraction [10]. They are:

$$\frac{d\phi_g}{dz} = \frac{\pi i}{\xi_g}\phi_0 e^{-2\pi i s z} + \frac{\pi i}{\xi_g}\phi_g. \qquad (3.12)$$

And

$$\frac{d\phi_g}{dz} = \frac{\pi i}{\xi_g}\phi_0 + \frac{\pi i}{\xi_g}\phi_g e^{2\pi i s z}. \qquad (3.13)$$

where ξ_0 and ξ_g are called the extinction coefficients for the direct and diffracted beam. From these equations, the amplitude of the diffracted beam continuously increases and decreases when the beam moves through the

specimen.

These equations are valid for a perfect crystal. For defects can be modified by introducing the displacement field R. It can be shown that the Howie-Whelan equations can be written as:

$$\frac{d\phi_g}{dz} = \frac{\pi i}{\xi_g}\phi_g + \frac{\pi i}{\xi_g}\phi_0 e^{-2\pi i(sz+g\cdot R)}. \quad (3.14)$$

And

$$\frac{d\phi_0}{dz} = \frac{\pi i}{\xi_0}\phi_0 + \frac{\pi i}{\xi_g}\phi_g e^{2\pi i(sz+g\cdot R)}. \quad (3.15)$$

Therefore, when the displacement field of a specific defect is known, the Howie-Whelan equations can be used to deduce the contrast formed by making a BF or a DF image using g.

Dislocations contribute to the plasticity of materials. Therefore a study of the deformation behavior of a crystalline material is essentially a study of the nucleation and propagation of dislocations. Thus it is important that a dislocation can be characterized by a vector, which called Burgers vector b. In the figure 3.1, schematic picture of an edge dislocation shows the Burgers vector. In a BF or DF image contrast arise because the planes around the dislocation are bent. Since the Bragg condition is relaxed, i.e. the reciprocal lattice points are actually reload, there will be contrast though the component

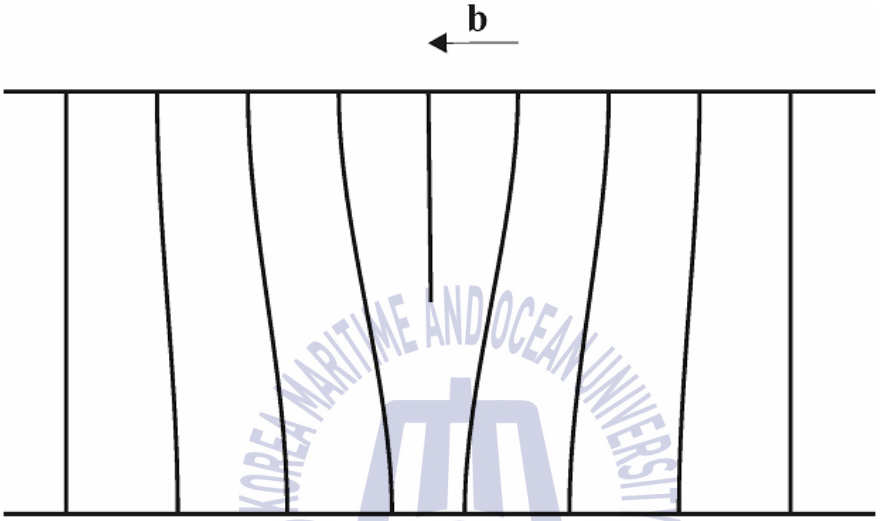

Figure 3.1 Schematic drawing of an edge dislocation with Burgers vector b.

of s is unequal to zero. The value of s changes by the bent planes, therefore the contrast changes and the dislocations can be seen as a line. When the specimen is tilted far away from the dislocation s slightly deviates from zero, the presence of the dislocation will bend the planes. In the BF or DF images, this effect gives rise to the bright-dark line pairs often seen.

For a screw type dislocation R is exactly parallel to the Burgers vector $\boldsymbol{b}$. For an edge type dislocation this is true to a first approximation. To determine the contrast caused by dislocations, the g·R product in the Howie-Whelan equations can be replaced by a term proportional to $\boldsymbol{g}\cdot\boldsymbol{b}$. It shows that dislocations give no contrast when:

$$\boldsymbol{g}\cdot\boldsymbol{b}=0 \qquad (3.16)$$

The planes around the dislocation are bent. This curvature can be used to attain a diffraction condition for which only the dislocation region is in Bragg condition.

This is called the invisibility criterion and it is used to determine the Burgers vector of a dislocation. By tilting the specimen different $\boldsymbol{g}$ vectors are used to image a dislocation and two reflections $\mathbf{g_1}$ and $\mathbf{g_2}$ can find for which the invisibility criterion holds, the Burgers vector may be determined using:

$$(\boldsymbol{g}_1\times\boldsymbol{g}_2)\parallel\boldsymbol{b}. \qquad (3.17)$$

When calculating the contrast by a dislocation, the width of the line contrast becomes smaller when s increases. This is called weak beam dark field imaging. When the s is very large it becomes sharp images of dislocations. Thus the sharp lines in the dark image are indicating the positions of the dislocations. This technique is especially useful when dislocations close to each other or when small dislocation loops is be identified. Figure 3.2 shows that the Ewald sphere passes almost through the 3**g** reflection then it becomes excited. However the image is made by the **g** reflection which becomes very weak because of the large value of s [10].

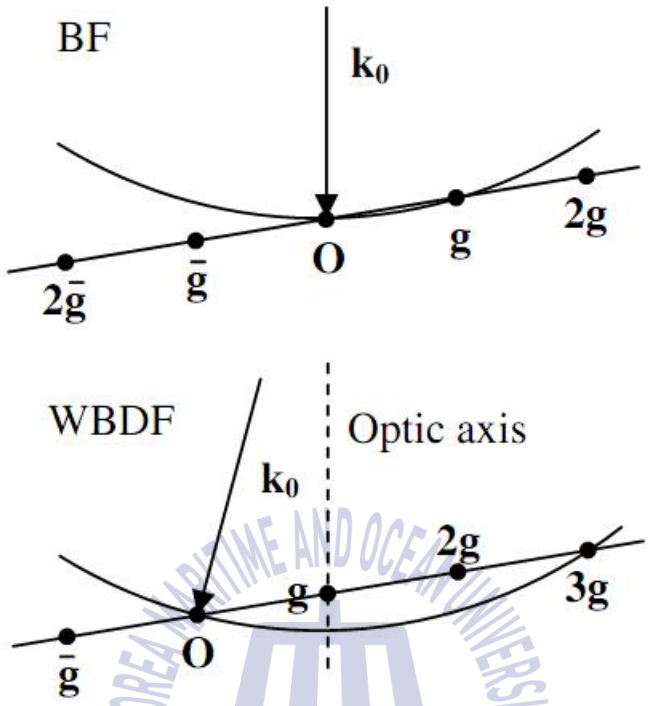

Figure 3.2 For weak-beam dark field imaging first a bright field two beam condition is set up (top). Next, the beam is tilted such that the initially bright g reflection is moved onto the optic axis. The Ewald sphere almost exactly crosses the 3g reflection, which therefore will be excited (bottom). The image is made using the now very weak g reflection.

3.3 Study on Microstructures of Light Emitting Diodes by Transmission Electron Microscopy

3.3.1 Analysis of Microstructure of GaN and Al_2O_3 Interface

The investigation of the crystallographic orientation relationship between the GaN film and the Al_2O_3 substrate was performed by bright field (BF) imaging and selected area diffraction. Figure 3.3 shows a BF-TEM image of the patterned Al_2O_3 substrate and the grown GaN. Figure 3.3 (b)–(d) shows selected area diffraction patterns (SADPs) of Al_2O_3, Al_2O_3 +GaN and GaN marked by Regions I, II and III in Fig. 3.3, respectively. The SADPs in Fig. 3.3(b)–(d) were taken along the [-12-10] zone axis of wurtzite GaN. The SADPs show a well-matched growth of the GaN along the *c*-axis 0001 of the Al_2O_3 substrate. The crystallographic relationship between the Al_2O_3 substrate and the GaN film was identified as $[-12-10]_{GaN}//[-1100]_{Al2O3}$, $(10-10)_{GaN}//(11-20)_{Al2O3}$. The crystallographic relationship between Al_2O_3 and GaN shows an in-plane atomic arrangement in the case of the 0001_{GaN} film grown on the (0001) substrate [14]. The rotation angle between the (1100) GaN film and the (1-100) Al_2O_3 substrate was estimated as 30° along with the Ga-plane of GaN on the O-plane of Al_2O_3. Therefore, the lattice mismatch between GaN (space group: P63mc) and Al_2O_3 (space group: R3c) is ~16% ($\Delta a=(a_{GaN}-a_{Al2O3}/\sqrt{3})/a_{Al2O3}/\sqrt{3}=0.16$, a_{GaN} = 3.1876Å and $a_{Al2O3}/\sqrt{3}$=2.749Å). To study the defect structure further at the various

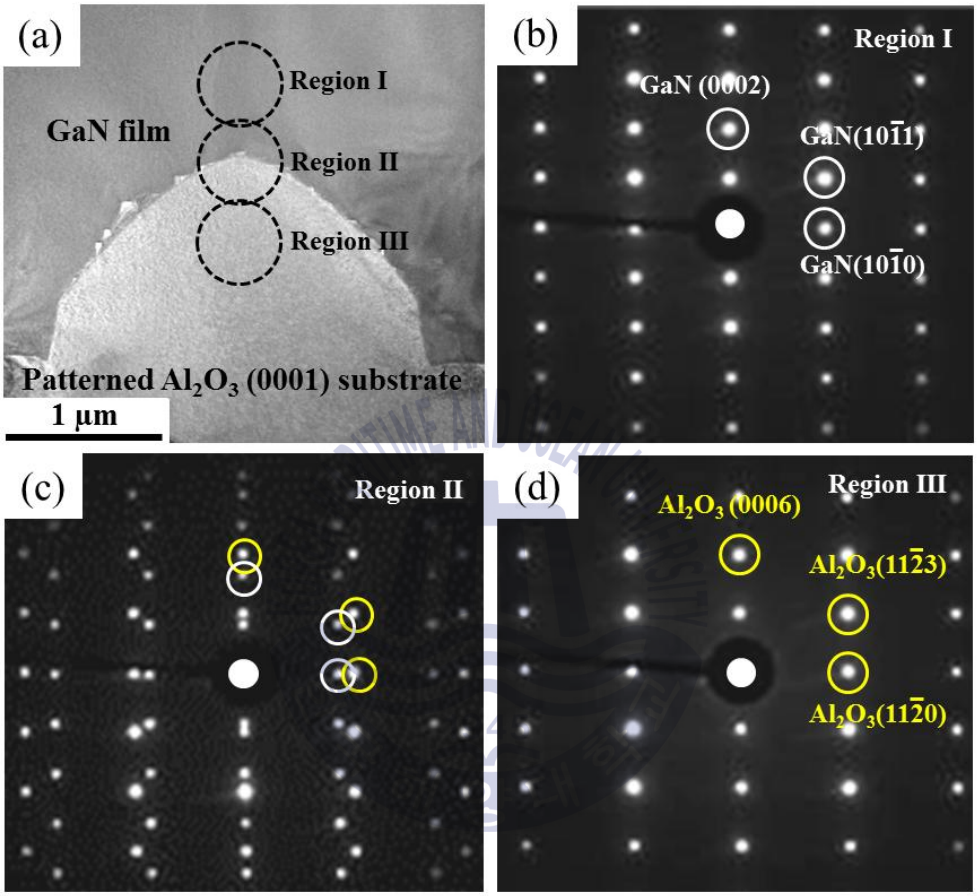

Figure 3.3 A cross-sectional BF-TEM image of the GaN film grown on the 0001 Al_2O_3 substrate

interfaces, the fiat surface (FS), vertical surface (VS), inclined surface (IS) and the top surface (TS) of the Al_2O_3 substrate (Regions I–IV in Fig. 3.4(a)) were separately analyzed by the HRTEM technique. Fig. 3.4(a) shows a magnified BF-TEM image recorded along $[11\text{-}20]_{GaN}$ in the interface between the GaN film and the Al_2O_3 substrate. Fig. 3.4(b) shows a HRTEM image of the FS area (Region I), in which the stacking faults were found in the GaN. Meanwhile, the MDs formed at the interface between the GaN film and the Al_2O_3 substrate were well characterized in the IFFT image (Fig. 3.4(b)) of diffraction spots $(10\text{-}10)_{GaN}$, $(11\text{-}20)_{Al2O3}$, $(-1010)_{GaN}$ and $(11\text{-}20)_{Al2O3}$ (indicated in Fig. 3.4(b)). The extra half-planes of MD on the substrate periodically existed as the hetero-junction structure with an interval of seven or eight $(11\text{-}20)_{Al2O3}$ lattice planes (16.1 Å or 18.4 Å, respectively), which agrees well with the average distance (D) between dislocations of 17.244 Å $D = d(10\text{-}10)_{GaN} \cdot d(11\text{-}20)_{Al2O3} / d(10\text{-}10)_{GaN} - d(11\text{-}20)_{Al2O3}$. Thereby, the lattice strain at the interface between the GaN film and the fiat Al_2O_3 substrate was almost relaxed by formation of MDs [15]. Figure 3.4(c) shows an HRTEM image of the VS area (Region II), where the ‘corner’ area was supposed to be formed from the lattice mismatch caused by the interaction between the growths of GaN initiated from the FS and the VS (as indicated by thick arrows). Fig. 3.4(d) shows an HRTEM image of the IS area (Region III), in which the recrystallized GaN (R-GaN) island was observed on the IS.

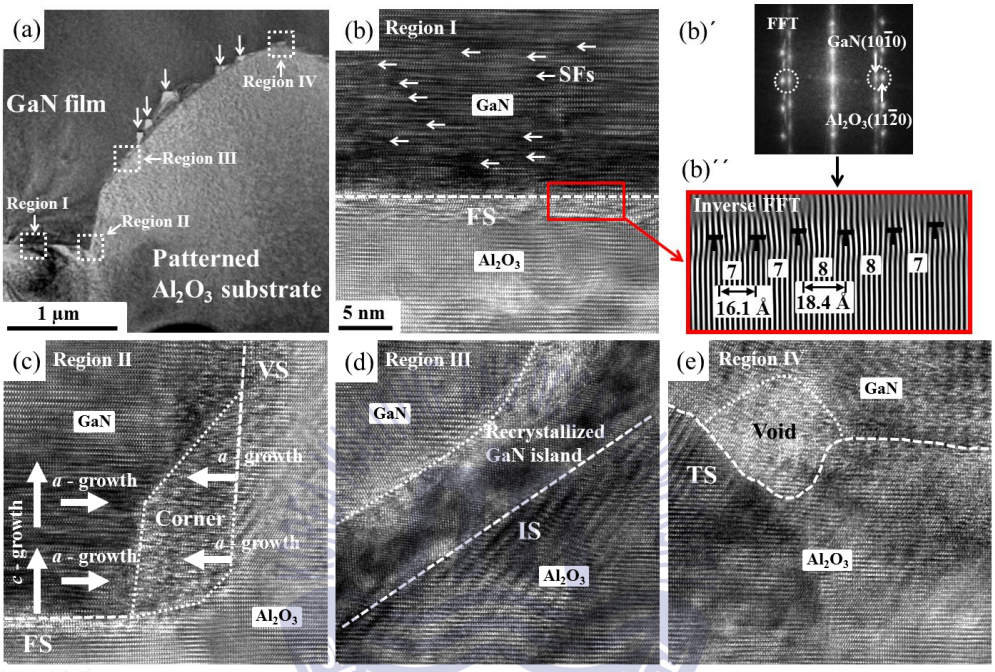

Figure 3.4 A cross-sectional BF-TEM image of the GaN film grown on the patterned Al_2O_3 substrate

Fig. 3.4(e) shows an HRTEM image of the TS area (Region IV), where nano-scale (~10 nm) void was formed between the GaN film and the substrate. Additionally, we found the void-like features on the IS of patterned Al_2O_3 (~100 nm, as marked by small arrows in Fig. 3.4(a)).

To investigate the R-GaN in detail, the crystallographic orientation relationship of the GaN film, the R-GaN island and the Al_2O_3 substrate in the IS area were analyzed by HRTEM, SADP and IFFT. Fig. 3.4(a) and (b) shows a locally magnified BF-TEM image of Fig. 3.4(a) and the corresponding SADP with the [-12-10] zone axis of GaN, respectively. Fig. 3.4(a) is the BF-TEM image, which clearly shows the morphology of the voids and the formation of R-GaN islands. Figure 3.5(b) shows two sets of diffraction patterns formed mainly by the GaN film and the Al_2O_3 substrate, and extra diffraction spots marked by vacant circles were also observed in SADP. These extra spots were originated from the R-GaN islands that had the [-1101] zone axis of GaN. The crystallographic orientation relationship of the GaN film, R-GaN and Al_2O_3 was identified as:

$$[\bar{1}2\bar{1}0]_{GaN\ film}//[\bar{1}101]_{R-GaN}//[\bar{1}100]_{Al_2O_3}, \quad (3.18)$$

$$(\bar{1}012)_{GaN\ film}//(1\bar{1}02)_{R-GaN}//(\overline{11}26)_{Al_2O_3}. \quad (3.19)$$

To investigate the rotation relationship further at the two interfaces of R-GaN, HRTEM and FFT/IFFT analyses were carried out in the interfaces of GaN/

R-GaN and R-GaN/substrate as marked by I and II in Fig. 3.5(a). We found that in the GaN/R-GaN interface, the intermediate layer of $(10\text{-}11)_{R\text{-}GaN}$ was rotated by 9° to $(0002)_{GaN}$ and also to $(0006)_{Al2O3}$ as indicated in Fig. 6c and d. The average values of $d(0006)_{Al2O3}$, $d(10\text{-}11)_{R\text{-}GaN}$ and $d(0002)_{GaN}$ were measured to be 2.2, 2.5 and 2.6 Å in Fig. 6c' and d', respectively. Therefore, it was revealed that the lattice mismatch between Al_2O_3 (0006) and GaN (0002) was reduced from 0.4 to 0.1 Å due to the insertion of R-GaN (2.2, 2.5 and 2.6 Å instead of 2.2 and 2.6 Å). In addition, it seems that the distance of $d(10\text{-}11)_{R\text{-}GaN}$ was enlarged at the interfaces by the 9° rotation to $(0006)_{Al2O3}$ and $(0002)_{GaN}$, which agrees well with previous study [16], resulting in further reduction of lattice mismatch at the interface of Al_2O_3/R-GaN and R-GaN/GaN. In short, the formation of R-GaN with the 9° to GaN and Al_2O_3 reduced the lattice mismatch between the Al_2O_3 substrate and the GaN film, resulting in the decrease in misfit dislocation from the GaN/R-GaN interface as indicated in Fig. 3.4(c) (marked by arrows) in comparison with the R-GaN/ Al_2O_3 interface as indicated in Fig. 3.4(d). From these results, it was suggested that the strain of the GaN film on the IS was relatively lower.

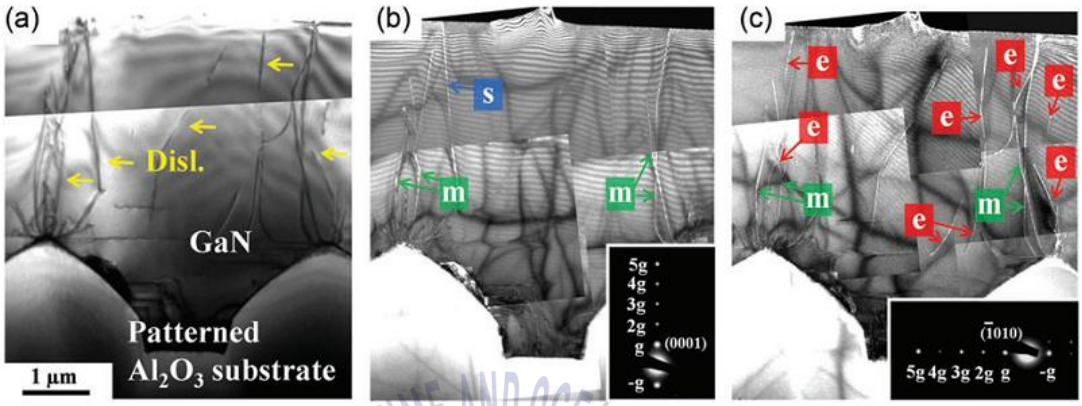

Fig. 3.5. (a) A BF-TEM image of the GaN film grown on the patterned Al_2O_3 substrate. (b) A weak-beam DF-TEM image taken in the diffraction condition of 5 g (g=0001) . (c) Aweak-beam DF-TEM image taken in the diffraction condition of 5 g g 1010 .

3.3.3 Analysis of Dislocations by Bright and Dark Fields Transmission Electron Microscopy Images

Figure 3.5 is the BF-TEM image recorded on the $[12\text{-}10]_{GaN}$ zone, showing the characteristics of dislocations extended from the substrate to the GaN film While a large number of TDs were observed in the TSs well as FS areas, they were scarcely observed in the IS area. Careful observation of the dislocation distribution of the TDs generated from the FS revealed that TDs were bent in the vicinity of IF and parallel to the interface of FS (similar to the results reported in ref. [17,18]). Thus, only a very small part of these TDs were propagated across the active layer to the GaN surface. On the other hand, most of the TDs generated from the TS were propagated to the GaN surface. Finally, total density of the TDs was shown to be significantly decreased by using the patterned substrate rather than the flat substrate. Determination of the type of dislocations generated from TS in the GaN film was carried out by means of a weak-beam dark-field (WBDF) technique. Figure 3.5(a) shows a BF image revealing the dislocations structures in the GaN film. WBDF images were obtained when 5g is excited, where g=(0001) and g=(-1010) as shown in Fig. 3.5(b) and c, respectively. In the case of perfect dislocations in hexagonal close-packed (HCP) structure, the burger vectors b of edge, screw and mixed dislocations were known as a=1/3<11-20>($\mathbf{b_e}$), c= <0001>($\mathbf{b_s}$) and a+c=1/3<11-23>($\mathbf{b_m}$), respectively [19-20].

Using the $\mathbf{g} \cdot \mathbf{b} = 0$ invisibility criterion assuming that the line directions of all the dislocations were vertical, the mixed dislocation at g=(0001) and g=(-1010) should be visible (Fig. 3.5 b and c) and the screw dislocation would be visible only at g 0001 (Fig. 3.5b), while the edge dislocations should be visible at g=(-1010) (Fig. 3.5c). It was found that the dislocations in the GaN film were predominantly edge type, which indicates high-level concentration of the stress at the apex regions of the Al_2O_3 cones [21]. Also, we could find out dislocation densities from the WBDF images. The densities of screw and edge dislocations were 3.4×10^6 cm^{-2} and 1.6×10^7 cm^{-2}, respectively. The densities of dislocations are similar or lower than reported values. The leakage current of GaN-based LEDs was reported to be considerably affected by the density of dislocations with a screw component [22,23]. Therefore, the LED efficiency could be improved by the usage of the cone-shaped embossed substrate, due to the dominance of edge-type dislocations.

3.4 Summary and Conclusion

In this chapter, the microstructural details of the GaN film grown on a cone-shaped patterned Al_2O_3 substrate were investigated using high-resolution transmission electron microscopy and weak-beam dark-field techniques. Various defects such as misfit dislocations (MDs), recrystallized GaN (R-GaN) islands and nano-voids were observed on the patterned Al_2O_3

surfaces, i.e. the flat surface (FS), the inclined surface (IS) and the top surface (TS), respectively. Especially, the crystallographic orientation of R-GaN between the GaN film and the inclined Al_2O_3 substrate was identified as $[-12-10]_{GaN}$ // $[-1101]_{R\text{-}GaN}$ // $[-1100]_{Al2O3}$, $(-1012)_{GaN}$ // $(1-102)_{R\text{-}GaN}$ // $(-1-126)_{Al2O3}$. In addition, a rotation by 9° between $(10-11)_{R\text{-}GaN}$ and $(0002)_{GaN}$ and between $(10-11)_{R\text{-}GaN}$ and $(0006)_{Al2O3}$ was found to reduce the lattice mismatch between the GaN film and the Al_2O_3 substrate. Many TDs in the GaN film were observed on the FS and TS of Al_2O_3. However, few TDs were observed on the IS. Most of the TDs generated from the FS of Al_2O_3 were bent to the inclined facet rather than propagating to the GaN surface, resulting in a reduction in the dislocation density. Most of the TDs generated from the TS of Al_2O_3 were characterized as edge dislocations.

REFERENCES

[1] S. Nakamura, M. Senoh, N. Iwasa, and S. Nagaham, *Jpn. J. Appl. Phys*. **34** L797 (1995).

[2] C. F. Lin, J. H. Zheng, Z. J. Yang, J. J. Dai, D. Y. Lin, C. Y. Chang, Z. X. Lai, and C. S. Hong., *Appl. Phys. Lett*. **88**, 083121 (2006).

[3] S. Watanabe, N. Yamada, M. Nagashima, Y. Ueki, C. Sasaki, Y. Yamada, T. Taguchi, K. Tadatomo, H. Okagawa, and H. Kudo, *Appl. Phys. Lett*. **83**, 4906 (2003).

[4] E. Woelk, G. Strauch, D. Schmitz, M. Deschler, and H. Jurgensen., *Mater. Sci. Eng. B*. **4,** 419 (1997).

[5] X. H. Huang, J. P. Liu, Y. Y., Fan, and J. J. Kong, *IEEE Photon. Technol. Lett*. **23**, 944 (2011).

[6] H. Gao, F. Yan, Y. Zhang, J. Li, Y. Zeng, and G. Wang, *Solid State Electron*. **52**, 962 (2008).

[7] H. C. Lin, R. S. Lin, J. I. Chlyi, and C. M. Lee, *IEEE Photon. Technol. Lett*. **20**, 1621 (2008).

[8] M. De Graef : *Introduction to Conventional Transmission Electron Microscopy.* Cambridge University Press, (2003)

[9] J. M. Cowley: *Diffraction Physics.* North-Holland, 2nd Edition, (1981).

[10] D. B. Williams and C. B. Carter : *Transmission Electron Microscopy*, Springer, 2nd Edition, (2009).

[11] F. H. Li and D. Tang. *Acta Crystallographica*, **A41**, 376 (1985).

[12] D. R. Denley and H. V. Hart. *Journal of Applied Crystallography*, **35**, 546 (2002).

[13] A. Howie and M.J. Whelan, *Proc. Roy. Soc.* **A263**, 217 (1691).

[14] K. Dovidenko, S. Oktyabrsky, J. Narayan, and M. Razeghi, *J. Appl. Phys*. **79** , 2439 (1996).

[15] D.A. Porter and K.E. Esterling: *Phase Transformations in Metals and Alloys*, Chapman & Hall, London, 2nd Edition.,

[16] J. -M. Yang, J. C. Park, D. G. Park, K. Y. Lim, S. Y. Lee, S. W. Park, and Y. J. Kim , *J. Appl. Phys*. **94**, 4198 (2003).

[17] J. Yang L. Ui. W. Lai, L. Hoantao, X. Guangyi, Z. Wei, and H. Yanjun, *In: Proc. Nano-Optoelectronics Workshop,* 216 (2007).

[18] K. Hiramatsu, K. Nishiyama, M. Onishi, H. Mizutani, M. Narukawa, A. Motogaito, H. Miyake, Y. Iyechika, and T. Maeda , *J. Cryst. Growth* **221**, 316 (2000).

[19] S. R. Agnew, J. A. Horton, and M. H. Yoo, *Metall. Trans. A*. **33**, 851 (2002).

[20] P. B. Hirsch, Z. Zhou, and D. J. H. Cockayne, *Philos. Mag*. **87**, 5421 (2007).

[21] Y. Y. Wong, E. Y. Chang,T. H. Yang, J. R. Chang, J. T. Ku, M. K. Hudait, W. C. Chou, M. Chen, and K. L. Lin., *J. Electrochem. Soc*. **157**, H746 (2010).

[22] J. W. P. Hsu, M. J. Manfra, R. J. Molnar, B. Heying and J. S. Speck, *Appl. Phys. Lett.* **81**, 79 (2002).

[23] D. S. Li, H. Chen, H. B. Yu, H. Q. Jia, Q. Huang, and J. M. Zhou, *J. Appl. Phys*. **96**, 1111 (2004).

Chapter 4 Quantitative Analysis of Indium Composition in InGaN/GaN Multi-Quantum Wells by High-Resolution Transmission Electron Microscopy and High Angle Annular Scanning Transmission Electron Microscopy

4.1 Introduction

III-nitride semiconductors have been investigated extensively because of their superior properties in the development of high-efficiency devices for various applications such as general illumination, biological sensors, and data storage.[1-4] Significant progress has been made in bright light-emitting diodes (LEDs) and laser diodes through the use of InGaN/GaN multi-quantum wells (MQWs) as active materials.[5] These materials have a high radiative recombination efficiency and are capable of emitting over a spectral range that almost covers the visible spectrum and extends into the ultraviolet region by control of In composition.[6] It is expected that this compound could be used in future to develop tunable optical devices because of its wide wavelength range.[7] Since bandgap is determined by In concentration, a direct determination of this composition is very important. And the inhomogeneity is often formed in InGaN/GaN system, it can be affect in device efficiency. Furthermore, the development of devices is tend to increasingly complex and minimized. Therefore the analysis method is necessary which can provide accurate information in complex and small

structure.

Typically, the analysis of In composition has been attempted by high-resolution X-ray diffractometry (HRXRD), Rutherford backscattering spectrometry (RBS), secondary-ion mass spectrometry (SIMS), etc.[8-10] RBS and SIMS are powerful methods for compositional analysis. HRXRD can be used to obtain lattice parameters with sub-angstrom sensitivity, and chemical composition is estimated indirectly by applying Vegard's law. [11] However the narrow width and complex structure of InGaN/GaN MQWs in LED devices make that the mentioned methods are difficult to analyze compositional analysis. High-resolution transmission electron microscopy (HRTEM) can be used for the direct imaging on the atomic scale. The HRTEM image is formed by interference of both transmitted beam and multiple diffracted beams and it contains structural information. Therefore the lattice image can determine lattice parameters through accurate measurement with subangstrom resolution by HRTEM. [12] Further, geometric phase analysis (GPA)[13] and peak finding methods [14], which are strain mapping methods based on the HRTEM technique, have been applied due to its accurate structural information. Thus HRTEM can be used to analyze composition when the structural information is matched the composition analysis. High-angle annual dark-field scanning transmission electron microscopy (HAADF-STEM) micrographs are formed by

incoherently scattered electrons as opposed to Bragg scattered electrons. This analysis technique is sensitive to variations in sample atomic number (Z-contrast images) [15] and HAADF-STEM can provide information on specimen composition. Thus, HRTEM and HAADF-STEM techniques can be very useful for analyzing In composition of InGaN[16-17]. Moreover these techniques are expected to be the most suitable methods for analyzing InGaN/GaN MQWs in LED devices with complex structure by directing observation.

In this chapter, we determined the quantitative In composition in InGaN/GaN MQWs in real LED devices using HRTEM and HAADF-STEM techniques. To confirm the reliability of the results, the In compositions of InGaN were measured by RBS and HRXRD.

4.2 Theoretical Background of Analysis of Indium Composition in InGaN/GaN Multi-Quantum well

4.2.1 Vegard's law and Hooke's law in the InGaN/GaN layer

Vegard's law

In materials science and metallurgy, Vegard's law is the empirical that the lattice parameter of a solid solution of two components is approximately equal to a rule of mixtures of the two components ' lattice parameters at the same temperature [11]:

$$a_{A_{(1-x)}B_x} = (1-x)a_A + xa_B. \qquad (4.1)$$

Vegard's law assumes that both components A and B have the same crystal structure. Here, $a_A x_B(1\text{-}x)$ is the lattice parameter of the solution, a_A and a_B are the lattice parameters of the pure components, and x is the molar fraction of B in the solution. Often deviations of Vegard's law from the linear behavior are observed. A detailed study of such deviations was carried out. For systems known to approximately yield to Vegard's law, the approximation may also be used to estimate the composition of a solution from knowledge of its lattice parameters. In many binary systems, the band gap in semiconductors is approximately a linear function of the lattice parameter. Therefore, if the lattice parameter of a semiconductor material follows Vegard's law, it is a linear relationship between the band gap and composition.

Hooke's law

Hooke's law is a principle of physics that states that the force F needed to extend or compress a spring by some distance X is proportional to that distance. That is: F = kX, where k is a constant factor characteristic of the spring: its stiffness, and X is small compared to the total possible deformation of the spring. Hooke's equation holds in many other situations

where an elastic body is deformed. This equation can be assumed for elastic body or material is linear-elastic..

Hooke's law is only a first-order linear approximation for springs and other elastic bodies to applied forces. It must finally fail once the forces surpass some limits, material can be compressed beyond a certain minimum size, or stretched beyond a maximum size. Many materials will deviate from Hooke's law before those elastic limits are reached. The relation between strain and stress for complex object can be deduced by Hooke's law.

4.2.2 High-Angle Annular Dark-Field STEM

Scanning Transmission Electron Microscopy

The STEM image is formed by scanning a probe (convergent beam) in a raster over the specimen and collecting the transmitted (figure 4.1). The magnification of image is determined by the scanned are. The intensity of the image is the total signal which is collected with a detector during the dwell time. This kind of serial imaging allows collection of different types of signals simultaneously, however the long scanning time makes that the process becomes very sensitive to mechanical and electrical disturbances. On the contrary in conventional TEM, the whole image is generated by parallel beam.

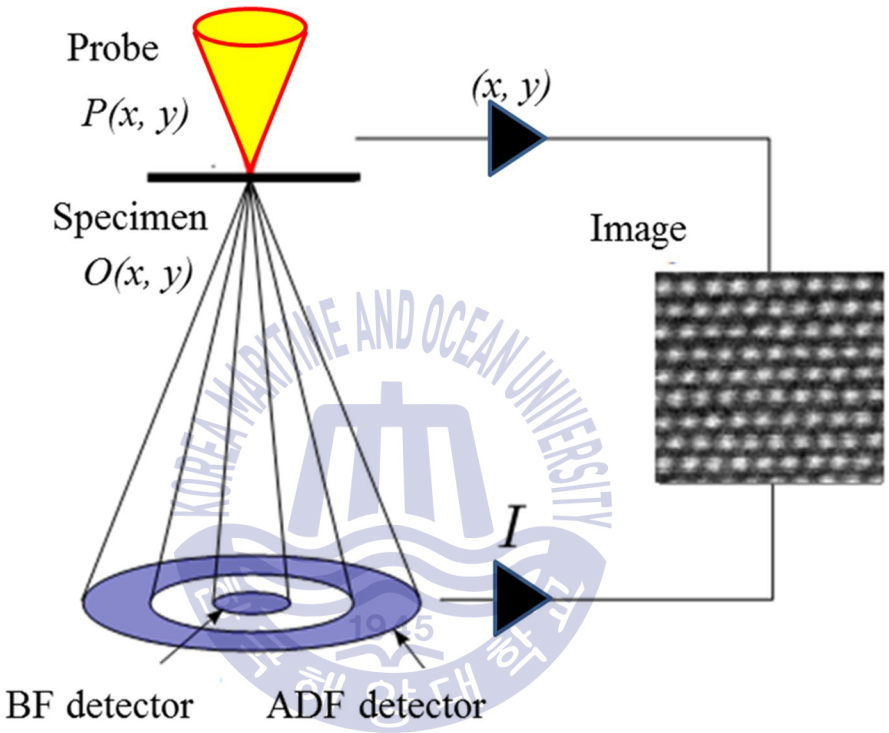

Figure 4.1 Operating principle of the STEM imaging system.

Detector geometries in STEM

BF imaging in STEM is performed by using a centered detector [18]. The size of the BF detector is that it picks the central disk of the CBED pattern. When the size of the condenser aperture is big enough to allow the disks to overlap, the BF STEM detector will capture scattering from both the direct and the overlapping diffracting disks. BF STEM contrast is equivalent to HRTEM image contrast under these conditions [19]. BF STEM images are hence coherent phase-contrast images. Annular BF (ABF) imaging use a small annular detector placed within the bright field cone, and visualizing light elements of these conditions BF STEM contrast is equivalent to HRTEM image contrast according to the principle of reciprocity [20]

Annular dark-field (ADF) images are formed by an annular detector, around the optical axis. The beam scattered to a certain angular range are collected. The BF detector sits in the center the annular detector. Thus BF and ADF images can be recorded simultaneously. High-angle ADF (HAADF) imaging is selecting an annular detector with a large inner and outer radius (typically from~30-50mrad ≥150 mrad,) in order to detect electrons scattered to high angles. The diffraction-contrast effects are minimized and incoherent images with intensity dependent on Z are obtained in HAADF imaging.

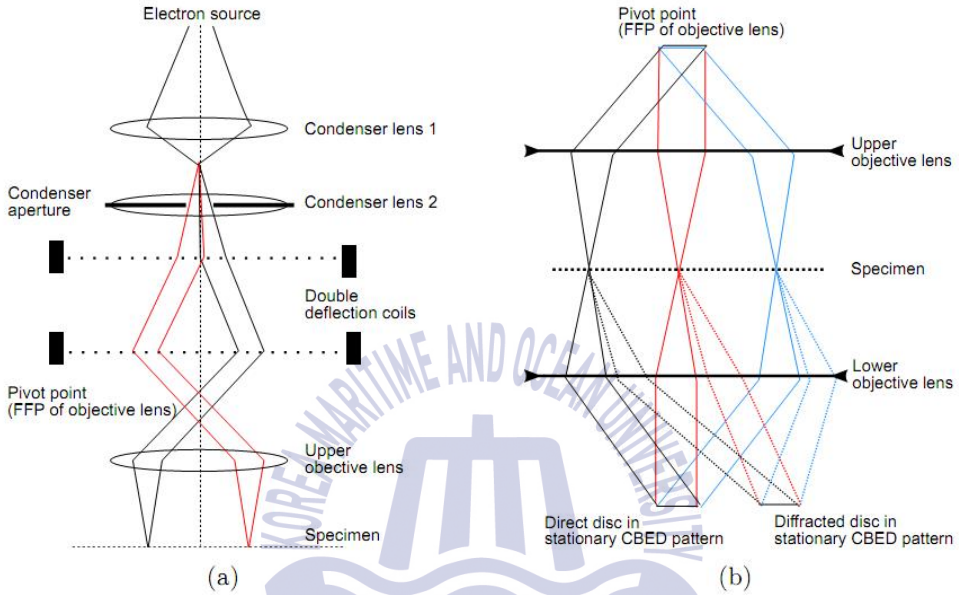

Figure 4.2 (a) Schematic of the STEM lens system and the scanning of a convergent probe and (b) a more detailed ray diagram for the specimen stage.

HAADF STEM image formation

From the image intensities, the Z-sensitivity allows compositional analysis at a high resolution. The imaging process can be described as incoherent, and the intensity of image becomes a convolution in intensity [21, 22]:

$$I_{incoh} = |P(R)|^2 \otimes |\psi(R)|^2 \qquad (4.2)$$

where P(R) is the function of the illuminating probe and (R) is the object wave-function. This is the mathematical definition for incoherent imaging. In HRTEM imaging is illuminated with a coherent plane wave. The image is formed from the exit-surface wave-function by the objective lens, which suffers from aberrations. The blurring effect of the lens aberrations can be described as a convolution with a point spread function (PSF) P(R), the intensity of result image becomes [23]

$$I_{coh} = |P(R) \otimes \psi(R)|^2, \qquad (4.3)$$

which is for coherent imaging.

$$I_{coh} = [P(R) \otimes \psi(R)] \cdot [P*(R) \otimes \psi*(R)], \qquad (4.4)$$

which shows that the convolution of (R) with the PSF and phase information are in complex amplitude and lost in the imaging process. Thus the resulting

coherent image intensity is sensitive.

4.3 Analysis of Indium Composition in InGaN/GaN single layers

First, we prepared thin InGaN layers with different In compositions for comparison with InGaN/GaN MQWs. Test samples A (T-A) and B (T-B) were grown on thick GaN films on a sapphire (0001) substrate by metal organic chemical vapor deposition. The thicknesses of the InGaN layers in T-A and T-B, as determined from TEM, were ~35.4 and ~37.8 nm, respectively. The samples were thick enough for measurement using RBS and HRXRD. HRXRD measurements and simulation of the T-A and T-B samples were performed to measure the In compositions quantitatively and the values obtained were compared with RBS results. HRXRD measurements were obtained using a Cu Kα X-ray source. The In composition in the InGaN layer from HRXRD results was simulated using the X'pert Epitaxy program. RBS was performed using a 1 mm collimated beam of 2.275 MeV^4 He^+ ions at 40 μC. Backscattered particles were detected at 160° with respect to the beam direction.

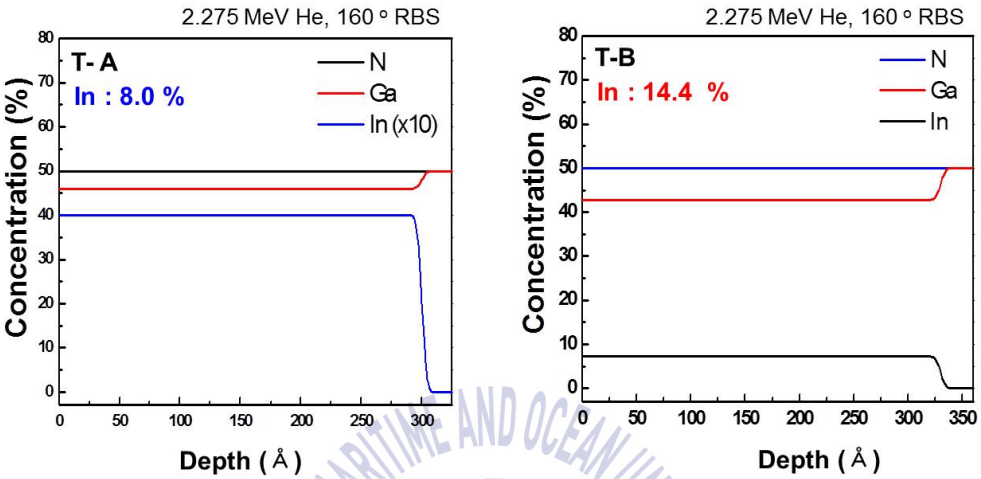

Figure 4.3 RBS results of T-A and T-B

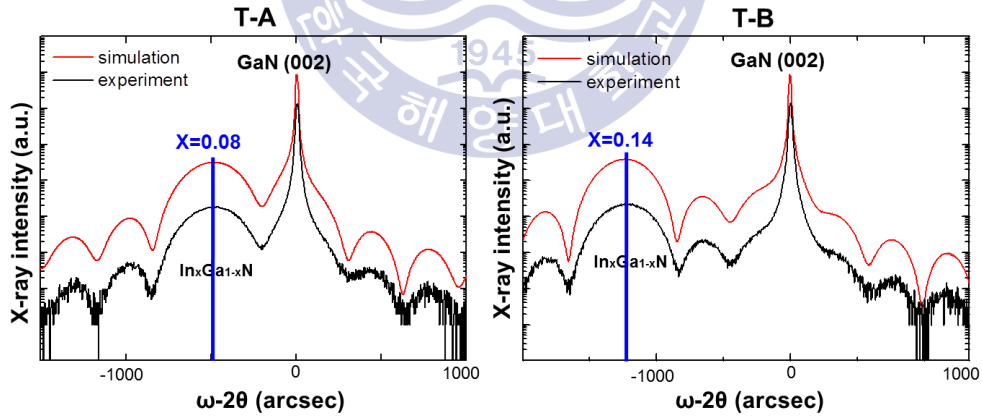

Figure 4.4 XRD results of T-A and T-B

4.3.2 X-ray Diffraction Studies

Figure 4.4 shows the measured and simulated $2\theta/\omega$ HRXRD spectra of the InGaN/GaN samples, T-A and T-B. Well-separated InGaN and GaN (002) peaks and layer thickness fringes were observed. When the epitaxial thin films have flat surfaces, in other words film thicknesses are not subject to random fluctuations. Then the contribution of scattering from the interface is reinforced and can often be observed as fringes in the diffraction pattern. These are termed thickness fringes. The spectra show that the InGaN layers have flat surfaces and are of uniform thickness. The peaks of maximum intensity are the GaN (002) peaks and the InGaN layer peaks of T-A and T-B are at $2\theta = 34.15°$ and 33.81°, respectively.

The lattice parameters can be calculated using Bragg's law, and data from the measured HRXRD spectra can be used to determine the In compositions. Any variation in composition is assumed to be linear, as in Vegard's law[14] :

$$c_{InGaN} = xc_{InN} + (1 - x)c_{GaN}. \qquad (4.5)$$

The variable x can be determined from:

$$x = \frac{(c_0 - c_{GaN})}{(c_{InN} - c_{GaN})}. \qquad (4.6)$$

This assumption may result in errors in calculation of the composition when the InGaN layers have a lattice strain with smaller thickness than the critical thickness.[24-25] In this case, the layer will be pseudomorphic and it is assumed that $a_{InGaN} = a_{GaN}$ and $c_{InGaN} > c_{GaN}$.

Figure 4.5 shows a plot of the *c*- versus *a*-lattice parameters for InGaN layers 30 nm thick. The filled squares and open circles indicated parameters as determined by HRXRD for InGaN layers with different In composition *x* and GaN layers from,[26] respectively. The InGaN layers are strained pseudomorphically to the in-plane lattice parameter of the GaN layer as confirmed by HRXRD. The unit cell is distorted in the biaxially strained wurtzite structure, InGaN/GaN. To differentiate between the effects of strain and composition on c_{InGaN}, both lattice parameters, a_{InGaN} and c_{InGaN}, must be measured. Then, *x* can be determined from Hooke's law [27,28]:

$$[c_{InGaN} - c_0(x) + 2\frac{C_{13}(x)c_0(x)}{C_{33}(x)a_0(x)}[a_{InGaN} - a_0(x)]] = 0 \quad (4.7)$$

where the subscripts 0 and InGaN are the relaxed and measured lattice parameters, respectively, and $C_{ij}(x)$ is the linearly interpolated elastic constant from the binary semiconductors. The variable *x* can be determined from Eq. (3). Linear interpolations between the *c*- and *a*-lattice parameters of unstrained GaN and InN yield the composition-dependent lattice parameters

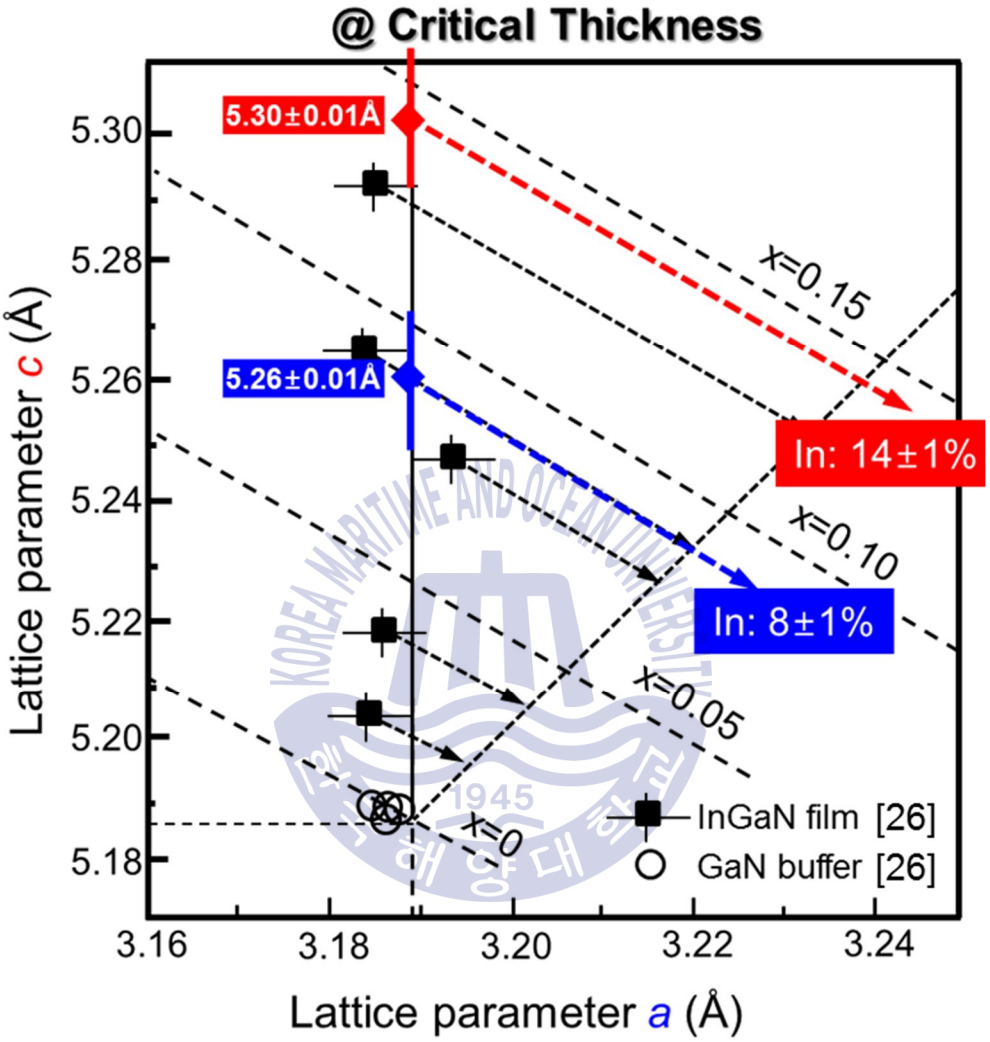

Figure 4.5 *c*-lattice versus *a*-lattice parameters as determined by HRXRD for 30 nm-thick InGaN layers (filled squares) with different In compositions x and GaN layers (open circles). For comparison, *c*-lattice and *a*-lattice parameters as observed by HRTEM for T-A, T-B (filled circles) and high-In region, low-In region in MQWs (filled diamonds) are also shown, respectively .

of the unstrained InGaN (indicated in Fig. 4.5 by the dotted lines). The effect of biaxial strain on *c* and *a* is indicated by dashed lines for In compositions of x = 0, 0.05, 0.10 and 0.15. To confirm the reliability of the calculated In compositions of the strained InGaN layers, the lattice parameters measured by HRXRD in Ref. 20 were projected parallel to the dashed lines onto the *c*-versus *a*-curve for unstrained InGaN, as indicated by the dashed arrow lines. The thicknesses of T-A and T-B as determined from TEM measurements were 35.4 nm and 37.8 nm, respectively, indicating that these layers are strained.[29] The *c*-lattice parameters of T-A and T-B as determined from HRXRD spectra were 5.247 Å and 5.299 Å, respectively, and the simulated In compositions were 8.0% and 14.0%. RBS was used for confirmation of the quantitative compositional analysis, and results indicate that the In compositions of T-A and T-B were 8.0% and 14.4%, respectively. These values agree well with the results from the HRXRD simulation. When the lattice parameters from Fig. 4.5 are applied, the In compositions are found to be ~ 7.5% and ~ 14% for T-A and T-B, respectively. Again, these results are similar to those from the HRXRD simulation and RBS. The In composition can therefore be determined accurately by measuring the *c*-lattice parameter.

4.3.3 High-Resolution Transmission Electron Microscopy Studies

HRTEM technique is the most powerful method available for the direct observation of atomic structure and is therefore usually used to determine lattice parameters. However when the thickness of HRTEM specimen is too thin, the elastic relaxation of strained structures can occur along the electron-beam direction.[30] F Hüe et al. reported that a 30 nm thickness TEM specimen is not sensitive in thin film relaxation induced by electron-beam. [31] Thus our specimen may not be affected the relaxation effect because the thickness is ~ 50 nm (which is measured by FIB-SEM during TEM specimen preparation). Figure 4.6 shows HRTEM micrographs of T-A and T-B. The calibration process is necessary for accurate lattice parameter determination. The lattice parameters were determined by measuring the intensity profile of HRTEM images in the Gatan program. The *c*-lattice parameter in the HRTEM images were calibrated by matching the known lattice parameter of GaN, 5.186 Å, as shown in Fig. 4.6 (b) and (d). The *a*-lattice parameters of the InGaN layers and GaN in Fig. 4.6 (a) and (b) were both 2.78 Å, because the layer thicknesses are less than the critical thickness. From the HRTEM images, we measured the six *c*-lattices spacing of InGaN. Then the *c*-lattice spacing was through directly comparing the six *c*-lattices spacing of GaN in the same image. The measuring was repeated several times and the results were averaged. The measuring accuracy was improved through directly

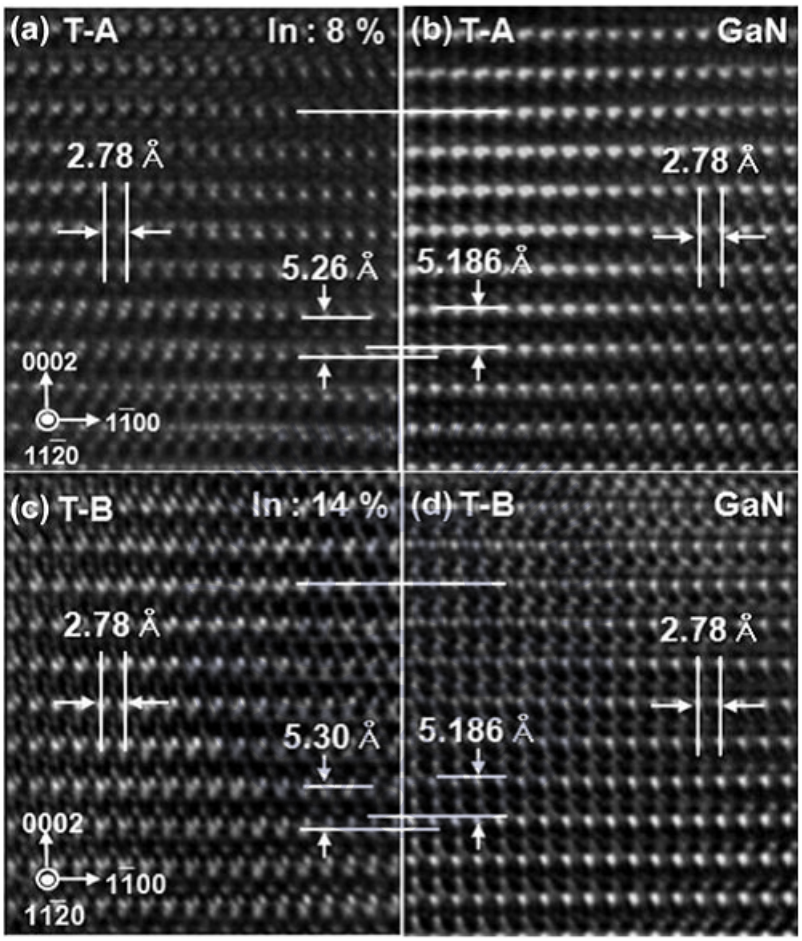

Figure 4.6. HRTEM images of (a, b) T-A and (c, d) T-B. The *c*-lattice parameter is 5.26 Å in T-A and 5.3 Å in T-B.

comparing several lattices in the same image taken with in-focus, so we could measure the minute differences of lattice constants. The *c*-lattice parameters in the InGaN layers were 5.26 Å and 5.30 Å for T-A and T-B, respectively, and which are shown in Fig. 4.5 with error bars (±0.01 Å). Using these lattice parameters, the In compositions were found to be ~8% and ~14% for T-A and T-B, respectively, from Fig. 4.5. These values are consistent with the HRXRD and RBS results.

4.4 Analysis of Indium Composition in InGaN/GaN Quantum Wells

4.4.1 High-Resolution Transmission Electron Microscopy Studies

HRXRD is commonly used for InGaN MQW characterization because it is difficult to analyze the composition of thin quantum well layers using other methods.[29] The use of HRXRD data for compositional analysis of InGaN/GaN MQWs is difficult because they are composed of complex multilayer structures such as in real LED devices. It was difficult to obtain an accurate In composition in the High- and Low-In regions for our InGaN/GaN MQWs from HRXRD because the spectra were not clear. We therefore attempted to determine the In composition of InGaN/GaN MQWs in LED devices through *c*-plane measurement in HRTEM. Figure 4.7 (a) shows a cross-sectional TEM image of InGaN/GaN MQWs. Figs. 4.7 (b) to (d) show enlarged images of InGaN/GaN MQWs, corresponding to the rectangular

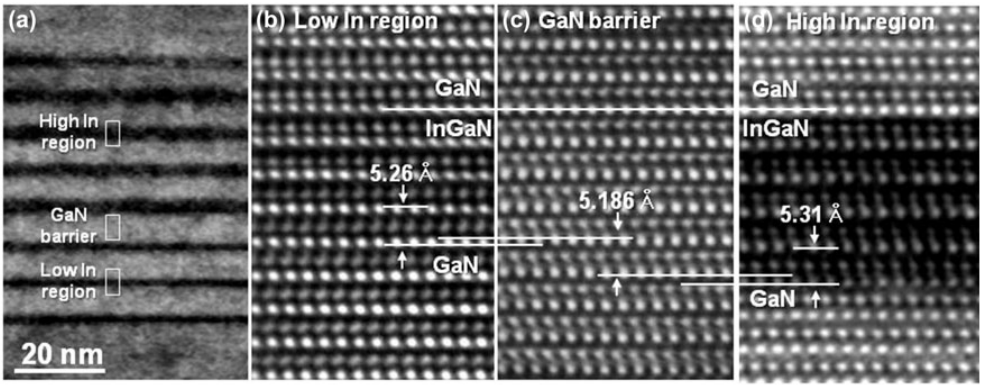

Figure 4.7 (a) TEM image of InGaN/GaN MQWs in LED device. (b–d) Enlarged HRTEM micrographs of the low-In region, GaN barrier, and high-In region MQWs. *c*-lattice parameters are 5.26, 5.186, and 5.31 Å, respectively.

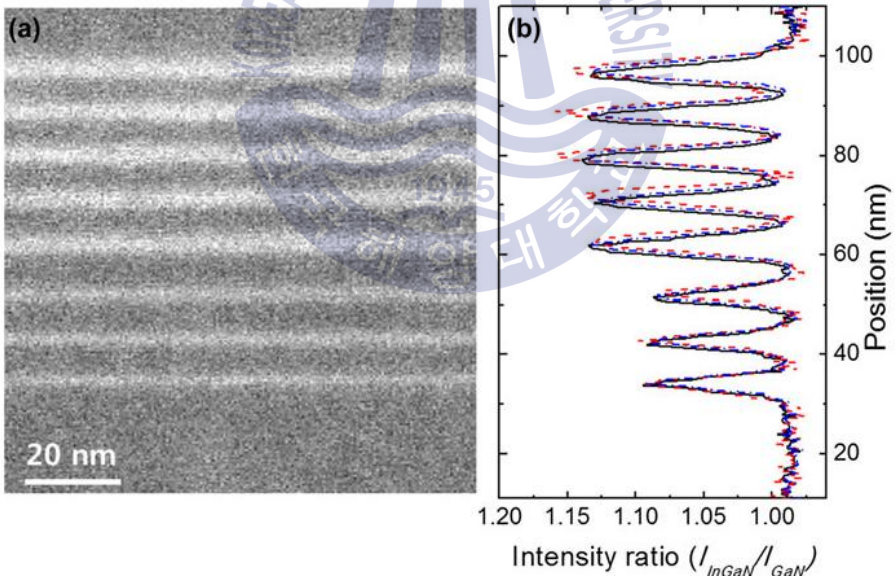

Figure 4.8 (a) HAADF-STEM image of InGaN/GaN MQWs and (b) HAADF-STEM intensity ratios of IInGaN/IGaN measured on InGaN/GaN MQWs.

regions in Fig. 4.7 (a). To minimize errors, the *c*-lattice parameters of the GaN region were fixed at 5.186 Å in Fig. 4.7 (c). And then, we measured the five *c*-lattices spacing of InGaN through directly comparing the five *c*-lattices spacing of GaN in the same HRTEM image. The *a*-lattice parameters in Fig. 4.7 (b) to (d) are identical to those in Fig. 4.5. The *c*-lattice parameters were measured to be 5.26 Å in the Low-In region (Fig. 4.7(b)) and 5.31 Å in the High-In region (Fig. 4.7(d)). Thus In compositions were found to be ~14.5% and ~8% for the High- In region and Low-In region, respectively, when the *c*-lattice parameters of in Fig. 4.7 were matched against Fig. 4.5. The results show that HRTEM can be the useful method for the compositional analysis of InGaN/GaN MQWs in the complex structure.

4.4.2 High-Angle Annular Dark-Field Images

We also conducted HAADF-STEM technique, which allows for the collection of electrons scattered at high angles by specimen nuclei, to form an incoherent image. According to Rutherford scattering, an atom contributes to image intensity in proportion to its atomic number Z raised to the power γ.[15] As a first approximation, since the image intensities are proportional to the integral of Z^{γ} ($1.6 \leq \gamma \leq 2$) along the beam direction, it is possible to discriminate between the intensity levels in the reconstruction between the different elements.[33] For InGaN, the gallium atom positions are occupied

by In atoms with large atomic number. Therefore, higher In compositions in the InGaN layers show a brighter contrast in the HAADF-STEM images compared with the lower In compositions. Figure 4.8(a) and (b) shows HAADF-STEM micrographs of InGaN/GaN MQWs and HAADF-STEM intensity ratio profiles of InGaN and GaN, respectively. The HAADF-STEM intensity profiles were measured on three times in the same specimen. The contrasts of High In and Low In regions show much difference and it shows dependence of ADF image contrast on $\sim Z^2$. However large differences exist in the intensity ratio at each measured images on the same condition. Figure 6 shows the In compositions in the High- and Low-In regions from the rate of increase in intensity that was calculated using Z^{γ} where $\gamma = 2$.[15] Differences of ~3% exist when the same exponent is used in Fig. 4.9.

The HAADF-STEM intensity can be influenced by various causes, such as electron beam damage, diffusion of In out of the sample during STEM observations, and ion beam damage during specimen preparation, etc.[34] The electron beam current was reduced below the maximum attainable from the microscope and was 35 Acm^{-2}.[35] This led to In clustering after 220 s, corresponding to a dose per area of 0.08 nC/nm2, but the dose of our experimental was lower than this value. Thus it is expected that influence of beam damage, such as In clustering, is not substantial in HAADF intensity. However, the background intensity can be increased caused by carbon

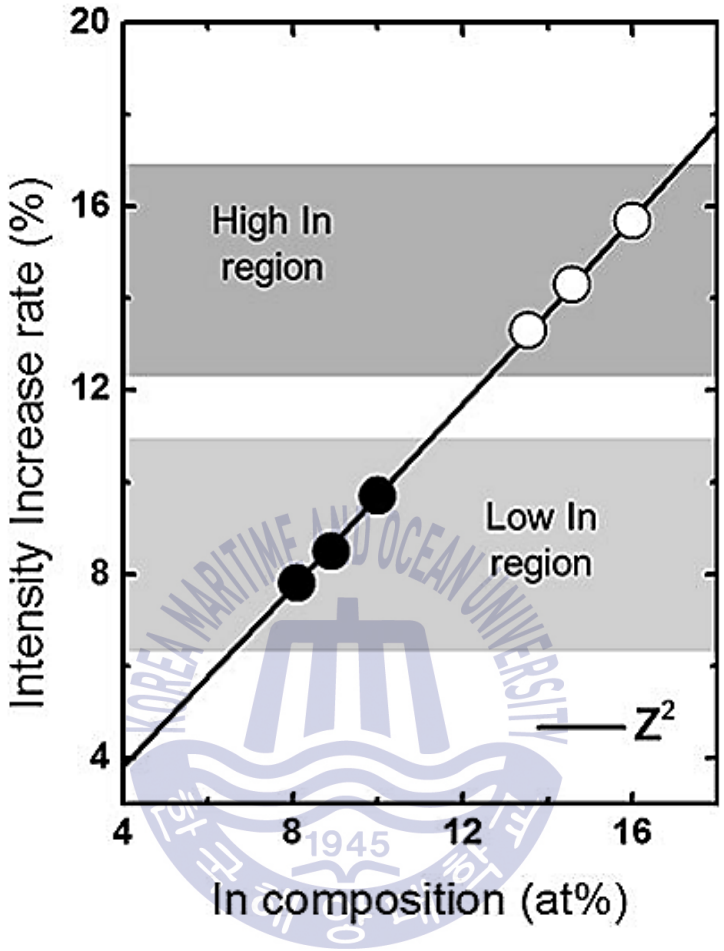

Figure 4.9. In compositions as determined from the rate of increase in HAADF-STEM intensity with exponent equal to 2 for the low-In region (filled circles) and high-In region (open circles).

contamination. This leads to a decrease of the intensity contrast between GaN and InGaN.[36] Also contrast variation can correspond to surface damage caused by ion-milling in the FIB preparation.[37] These results suggest that a quantitative evaluation of In composition is difficult, whereas a relative comparison is possible using the HAADF-STEM intensity.

4.5 Summary and Conclusion

In this chapter, we determined the quantitative composition of In in InGaN/GaN MQWs by using HRTEM and HAADF-STEM techniques. The In compositions of the InGaN layers in the test samples (T-A and T-B) were found to be ~8.0% and ~14.0%, respectively, from HRXRD; the results were confirmed by RBS. The quantitative In compositions in T-A and T-B were determined from TEM, and the results are similar to those from HRXRD and RBS. Quantitative In compositions can therefore be determined reliably using HRTEM technique. The In composition in InGaN/GaN MQWs of a real LED device were determined using HRTEM and were found to be ~14.5% and ~8.0% for the High-In and Low-In regions, respectively. The HAADF-STEM study showed relative composition differences because the quantitative In composition could not be determined because of problems such as differences in specimen thickness, carbon contamination, and ion beam damage during specimen preparation.

REFERENCES

[1] S. Nakamura, M. Senoh, S. Nagahama, N. Iwasa, T. Yamada, T. Matsushita, Y. Sugimoto, and H. Kiyoku, *Appl. Phys. Lett*. **69**, 3034 (1996).

[2] H. Morkoç, S. Strite, G. B. Gao, M. E. Lin, B. Sverdlov and M. Burns, *J. Appl. Phys*. **76**, 1363 (1997).

[3] S. J. Pearton, B. S. Kang, S. Kim, F. Ren, B. P. Gila1, C. R. Abernathy, J. Lin, and S. 0. G. Chu, *J. Phys.: Condens. Matter* **16**, R961 (2004).

[4] I. K. Shmagin, J. F. Muth, R. M. Kolbas, R. D. Dupuis, P. A. Grudowski, C. J. Eiting, J. Park, B. S. Shelton and D. J. H. Lambert, *Appl. Phys. Lett*. **71**, 1382 (1997).

[5] M. D. McCluskey, L. T. Romano, B. S. Krusor, N. M. Johnson, T. Suski and J. Jun, *Appl. Phys. Lett.* **73**, 1281 (1998).

[6] I. K. Shmagin, J. F. Muth, R. M. Kolbas, R. D. Dupuis, P. A. Grudowski, C. J. Eiting, J. Park, B. S. Shelton and D. J. H. Lambert, *Appl. Phys. Lett*. **71**, 1382 (1997).

[7] K. S. Ramaiah, Y. K. Su, S. J. Chang, B. Kerr, H. P. Liu and I. G. Chen, *Appl. Phys. Lett*. **84,** 3307 (2004).

[8] S. Pereira, E. Pereira, E. Alves, N. P. Barradas, K. P. O'Donnell, C. Liu, C. J. Deatcher and I. M. Watson , *Appl. Phys. Lett*. **81**, 2950 (2002).

[9] L. Marona, P. Perlin, R. Czernecki, M. Leszczyński, M. Boćkowski, R. Jakiela, T. Suski and S. P. Najda, *Appl. Phys. Lett*. **98**, 241115 (2011).

[11] C.G. Van de Walle, M.D. McCluskey, C.P. Master, L.T. Romano, and N.M. Johnson, *Mat. Sci. Eng. B* **59**, 274 (1999).

[12] C. Kisielowski, C.J.D. Hetherington, Y.C. Wang, R. Kilaas, M.A. O'Keefe, A. Thust, *Ultramicroscopy* **89**, 243 (2001).

[13] J. Li, C. Zhao, Y. Xing, S. Su, and B. Cheng, *Materials* **6**, 2130 (2013).

[14] P. L. Galindo, S. Kret, A. M. Sanchez, J. Laval, A. Yáñez, J. Pizarro, E. Guerrero, T. Ben, and S. I. Molina, *Ultramicroscopy* **107**, 1186 (2007).

[15] S.J. Pennycook, S.D. Berger, and R.J. Culbertson, *J. Microsc*. **144**, 229 (1986).

[16] T. Schulz, T. Remmele, T. Markurt, M. Korytov and M. Albrecht, *J. Appl. Phys*. **112**, 033106 (2012).

[17] T. Walther, H. Amari, I.M. Ross, T. Wang, and A.G. Cullis, *J. Mater. Sci*. **48**, 2883 (2013).

[18] D. B. Williams and C. B. Carter: *Transmission Electron Microscopy*, Springer, 2nd ed., (2009).

[19] J. M. Cowley, *Appl. Phys. Lett*., **15**, 58 (1969).

[21] H. L. Zhou, T. B. Hoang, D. L. Dheeraj, A. T. J van Helvoort, L. Liu, J. C. Harmand, B. O. Fimland and H. Wema.,*Nanotechnology*, **20**, 415701 (2009).

[22]A. V. Crewe, J. Wall, and J. Langmore, *Science* **168**, 1338 (1970).

[23]P. Nellist and S. Pennycook, *Adv. Imag. Elect. Phys*., **113,** 147 (2000).

[24] S. Pereira, M. R. Correia, E. Pereira, K. P. O'Donnell, E. Alves, A. D. Sequeira and N. Franco., *Appl. Phys. Lett*. **79** , 1432 (2001).

[25] S. Srinivasan, R. Liu, F. Bertram, F.A. Ponce, S. Tanaka, H. Omiya and

Y. Nakagawa, *Phys. Status Solidi b* 2**28**, 41 (2001).

[26] J. Wagner, A. Ramakrishnan, D. Behr, M. Maier, N. Herres, M. Kunzer, H. Obloh and K.-H. Bachem, *MRS Internet J. Nitride Semicond. Res*. **4S1**, G2.8 (1999).

[27] S. Pereira, M. R. Correia, T. Monteiro, E. Pereira, E. Alves, A. D. Sequeira and N. Franco., *Appl. Phys. Lett*. **78**, 2137 (2001).

[28] M. R. Correia, T. Monteiro, E. Pereira, M.R. Soares, E. Alves., *J. Cryst. Growth* **230**, 448 (2001).

[29] K. P. O'Donnell, J. F. W. Mosselmans, R. W. Martin, S. Pereira and M. E. White*, J. J. Phys.: Condens. Matter* **13**, 6977 (2001).

[30] T. Niermann, J. B. Park, and M. Lehmann, *Ultramicroscopy* **111**, 1083 (2011).

[31] A. Pretorius, K. Müller, T. Yamaguchi, R. Kröger, D. Hommel, and A. Rosenaue., *Springer Proceedings in Physics* **120,** 17 (2008).

[32] F. Hüe, M.J. Hÿtch, J. -M. Hartmann, Y. Bogumilowicz, and A. Claverie, *Springer Proceedings in Physics* **120**, 149 (2008).

[33] D.E. Jesson, and S. Pennycook, *Proc. Roy. Soc. London* **A449**, 273 (1995).

[34] R. F. Egerton, P. Li, and M. Malac. *Micron* **35**, 399 (2004).

[35] T. M. Smeeton, M. J. Kappers, J. S. Barnard, M. E. Vickers, and C. J. Humphreys, *Appl. Phys. Lett.* **83**, 5419 (2003).

[36] A. Rosenauer, T. Mehrtens, K. Müller, K. Gries, M. Schowalter, P.V. Satyam, S. Bley, C. Tessarek, D. Hommel, K. Sebald, M. Seyfried, J. Gutowski, A. Avramescu, K. Engl, and S. Lutgen, *Ultramicroscopy* **111**, 1316 (2011)

[37] K. H. Baloch, A. C. Johnston-Peck, K. Kisslinger, E. A. Stach, and S. Gradečak. *Appl. Phys. Lett*. **102,** 191910 (2013).

Chapter 5 Strain Analysis of InGaN/GaN Multi-Quantum Wells by Dark-Field Electron Holography

5.1 Introduction

Strain is an important issue in the semiconductor industry because the strain is a great influence on the performance of electronic devices [1,2,3]. Strain affects the mobility of carriers, either electron or holes, besides the strain become the cause of defects. Therefore, in order to better understand and improve the properties of these device, it is necessary to have accurate information strain fields and process-induced strain [4,5]. There are many different methods to measure strain in semiconductors, such as X-ray diffraction [6] and micro-Raman Spectroscopy [7]. They are established techniques which now can be used to map strain, but only at the micron scale with spatial resolution for tens of nanometers. At smaller scale, transmission electron microscopy (TEM) based on techniques such as convergent beam electron diffraction (CBED) [8-10], nano beam electron diffraction (NBD) [11], high-resolution transmission electron microscopy (HRTEM) with geometric phase analysis (GPA) [12], and dark-field electron holography (DFEH) [13,14], have been used to provide information about train in semiconductor devices.

Béché *et al*. [14] mentioned different TEM techniques for strain

measurements at the nanoscale. CBED is very useful for strain analysis, with the best strain precision among all methods of measurement. However, CBED can sometimes be too sensitive to foil bending in the highly strained areas typical of devices [15] and cannot combine the necessary spatial resolution, precision, and field of view. NBD can provide strain maps, but the amount of obtained data will strongly limit the size of the map and the analysis process will be very time-consuming. HRTEM is an easy method combined with the image processing technique of GPA, which can measure local strains. Recently, Hytch *et al*. [13] reported dark-field electron holography, as an alternative method for measuring strain. This new technique has emerged as a powerful tool for mapping strain at the nanoscale by measuring the geometric phase of diffracted beam. The technique has been applied to the study of a variety of semiconductor nanostructures, ranging from a single layer to multilayers with thin and thick layers [11]. Based on the off-axis electron holography with medium high-resolution magnification, DFEH is to use an electron biprism to overlap a strained region of the device with an unstrained region. By selecting a specific diffracted beam with an objective aperture to obtain a dark-field hologram, the difference of lattice constant between strained and unstrained regions can be measured and the change of lattice constant can be mapped out through a data processing [16].

In this chapter, using DFEH with medium high-resolution magnification mode, we carry out the strain distributions in the InGaN/GaN MQWs. This includes phase reconstruction and interpretation of the strain maps, which can help other microscopist use this technique with medium high-resolution magnification mode.

5.2 Theoretical Background of Strain in InGaN/GaN Multi-Quantum well

5.2.1 Effect of Strain in Multi-Quantum Well

The strain has great effects on the formation of the InGaN islands and capping in different materials. Determination of the strain in the islands can result in their composition. Because of difference in the lattice parameters of GaN and InN, InGaN films epitaxially grown on a GaN buffer layer are strained. When the $In_xGa_{(1-x)}N$ is grown on the *c*-GaN in *c*-direction [0001], the in-plane lattice parameter a InGaN is compressed trying to match to the buffer lattice parameter a GaN as shown in the Fgure 5.1, while the out-of-plane lattice parameter of c_{InGaN} is expanded. The values of the strain and the lattice parameters depend on the indium content *x*. Hooke's Law can describe the stress tensor:

$$\sigma_i = \sum_j C_{ij} \in_j, \quad i,j = \{1, \dots, 6\}, \qquad (5.1)$$

where *Cij* and ϵ_j are the elastic constants and the strain components, respectively. The elastic constants also depend on the indium content *x* . For isotropic biaxial strain ($\epsilon_1 = \epsilon_2$) perpendicular to the c-axis, the wurtzite basal plane is isotropic, thus the strain component in the growth direction ϵ_2 and components in the basal plane (ϵ_1 and ϵ_2) can be written as [17]:

$$\epsilon_3 = -\frac{C_{13}}{C_{33}}(\epsilon_1 + \epsilon_2) = -2\frac{C_{13}}{C_{33}}\epsilon_1. \qquad (5.2)$$

The out-of-plane strain ($\epsilon_3 \equiv \epsilon_\perp$) and in-plane strain ($\epsilon_1 \equiv \epsilon_\parallel$) are defined as [18]

$$\epsilon_\perp = \frac{c-c_0}{c_0} \qquad \epsilon_\parallel = \frac{a-a_0}{a_0}, \qquad (5.3)$$

with a and c are the strained lattice parameters and a_0, c_0 are the relaxed ones:

$$\frac{c-c_0}{c_0} = -2\frac{C_{13}}{C_{33}}\frac{a-a_0}{a_0} = \quad -D(x)\frac{a-a_0}{a_0}, \qquad (5.4)$$

where D(*x*) is the distortion factor [18]

$$D(x) = -\frac{\epsilon_\perp}{\epsilon_\parallel} = \frac{2v}{1-v}. \qquad (5.5)$$

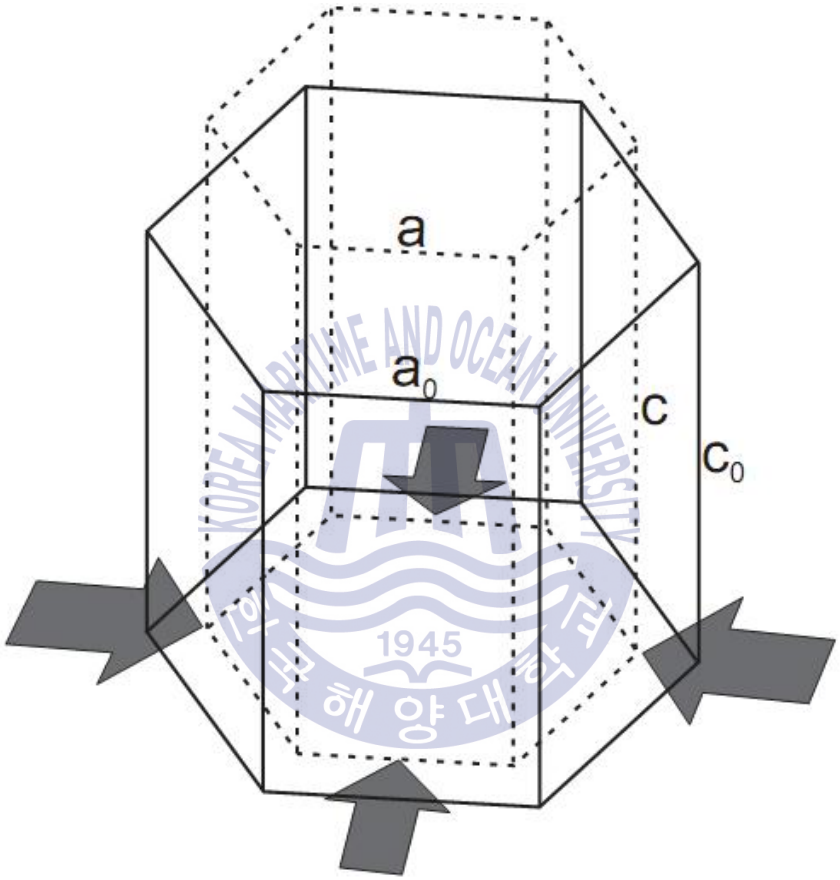

Figure 5.1 InGaN unit cell under biaxial strain in the basal plane a and c is strained unit cell parameters, while a_0 and c_0 are bulk (relaxed) values.

5.2.2 Dark-Field Electron Holography

Electron holography has been used for an widening range of applications since invented by Gabor [19]. The measurement of the wave phase allows the determination of the aberrations of the optical system. It has been perfected in the field of high-resolution off-axis electron holography [20-21]. In the medium-resolution, the phase measurement of the transmitted beam with the vacuum, electron holography has been used to confirm the existence of the phase change by the magnetic vector potential. Thus local in-plane projection of the magnetic field can be determined [21], which has led to the development for the study of magnetic fields at the nanoscale [22] and direct comparisons with micromagnetics modelling [23]. Also, the phase changes because of electrostatic fields have been studied by medium-resolution holography, by the measurement of potentials of materials, potential drop across p–n junctions, dopant concentrations in semiconductors.

Geometric phase can be measured and quantified by electron holography using the dark-field electron holography (DFEH). The geometric phase is only present in the diffracted beams. Therefore it cannot be measured by the conventional off-axis electron holography setup (Fig. 5.2). The crystal is oriented to one of the lattice planes in diffraction conditions and the illumination tilted so the emerging diffracted beam is aligned with the optic axis, as for conventional dark-field imaging, and an objective aperture

applied to prevent the other diffracted beams. A hologram is formed from the interference between the diffracted beam originate from an unstrained region of crystal, which as the reference, and a beam from the region of strained crystal. The relative phase of the diffracted beam between the two regions can be determined from the dark-field hologram. If the specimen thickness is uniform, the amplitudes of the two beams will be the same and the holographic fringe contrast is maximized. To measure the geometric phase component, the other phase terms, must be eliminated. To a first approximation, , crystalline and electrostatic phase do not depend directly on the local strain. Therefore, a direct measurement of geometric phase can be obtained by cancel of these terms if the sample is uniformly thick. For the measurement of strain, which depends on the phase gradient, the gradient of the non-geometric phase terms has to be zero, or the gradient of the difference. For the constancy of the crystal-line phas, the diffraction conditions also must be uniform over the two regions. Regions which exhibiting bend contours should be provented. It is more complex in the presence of compositional variations. Localized phase changes can occur at interfaces, therefore it is difficult to eliminate from the analysis. The measurement also can provide the relative distortion of the reference lattice. Therefore, a strict strain analysis requires the reference region to be unstrained, or errors will arise.

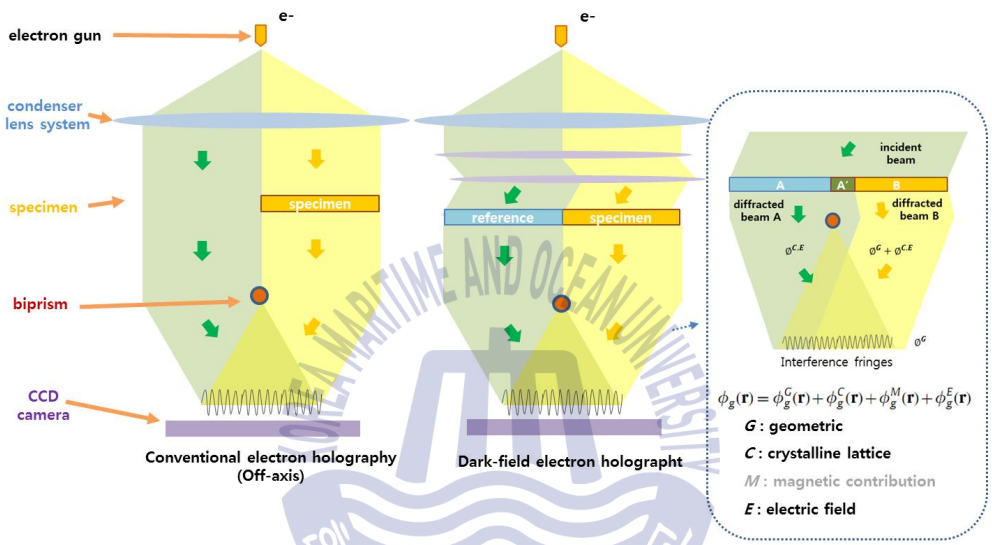

Figure 5.2 Off-axis electron holography schemes: (a) conventional setup with specimen (O) and reference (vacuum); (b) dark-field holography with strained crystal (B) and unstrained crystal (A). (c) a diffracted beam from an unstrained region of crystal (in green) is interfered with the same diffracted beam emanating from the region of interest (in yellow) with aid of biprism wire (red).

5.3 Analysis of Strain in InGaN/GaN Quantum Wells

5.3.1 Strain Analysis by High-Resolution Transmission Electron Microscopy

In the chapter 4, we obtained indium composition from lattice constant in the HRTEM image. The indium composition of high In region was 14.5 % and the *c*-lattice constant was 5.31 Å. However, the lattice constant is strained value because the thickness is less than critical thickness. It is essential original value of *c*-lattice constant of InGaN to calculate strain. The c-lattice constant of InGaN can be obtained from the equation:

$$a_{InGaN} = x \cdot a_{InN} + (1 - x)\, a_{GaN} \quad (5.6)$$

And unstrained *c*-lattice constant (In composition : 14.5 %) was obtained as 3.24 Å.

The strain of InGaN/GaN MQWs can be calculated from the equation:

$$\varepsilon = \frac{\Delta L}{L_0} = \frac{L - L_0}{L_0} \quad (5.7)$$

And the strain was calculated as 1.65 %.

5.3.2 Dark-Field Electron Holography Studies

In this study, the results were obtained by using a 200 kV FE-TEM (JEM-ARM200F) microscope equipped with a biprism. For holography, there are three special holographic modes including HOLO-L (HOLO-Dual),

HOLO-M and HOLO-H modes, which were designed as the names imply for low, medium and high-resolution magnification, respectively. For HOLO-M mode, the available magnification range is between 100k and 300k, and which is suitable for holography measurement of our samples. Therefore, this mode could be used in this study. The biprism was biased with the voltage of 25 V. The interference fringe spacing was measured to be 0.38 nm in the reference region. The width of the biprism and the fringe visibility were 35 nm and 13-19%, respectively. The specimen was oriented to a two-beam condition close to the [0001] zone axis in order to obtain a (0002) diffraction spot. Holograms were acquired with a 2k x 2k CCD camera (US1000). The phase images were reconstructed using the HoloDark plug-in installed in the DigitalMicrograph (Gatan) program. 2-D strain maps of the thin InGaN layer were derived based on phase images reconstructed from the hologram.

In order to obtain the 2-D strainmaps using the DFEH technique along the [0001] growth direction of InGaN/GaN, we obtained a dark field hologram at the (0002) diffraction spot. The dark-field hologram from this spot, with an electron bias voltage of 25 V is illustrated in Fig. 5. 3a. The intensity distribution of a dark-field hologram can be defined [24]:

$$I_{DFEH}(\vec{r}) = A_{GaN}^2 + A_{ROI}^2(\vec{r}) + 2\mu A_{GaN} A_{ROI}(\vec{r}) cos\left[\Delta\emptyset(\vec{r}) + 2\pi(\vec{q}_c + \vec{\Delta}g(\vec{r}).\vec{r}\right] \quad (5.8)$$

where $\vec{r}$ is the position vector in the recorded image. A_{GaN} and A_{ROI} are the amplitude of the waves diffracted by silicon substrate and the region of interest (InGaN). $\Delta\emptyset(\vec{r}) = \emptyset_{GaN} - \emptyset_{InGaN}(\vec{r})$ is the phase difference of the two diffracted waves. μ is the contrast and q_c the carrier frequency. $\vec{\Delta}g(\vec{r}) = \vec{g}_{GaN} - \vec{g}_{InGAN}(\vec{r})$ is the difference of the reciprocal lattice vectors which characterize the crystal structure in the two regions. The phase image obtained after reconstruction is defined $\emptyset(\vec{r}) = \Delta\emptyset(\vec{r}) + 2\pi\vec{\Delta}g(\vec{r}).\vec{r}$. The strain can be calculated from the phase gradient $\Delta\emptyset(\vec{r}) = 2\pi\vec{\Delta}g(\vec{r}).\vec{r}$ in the regions where term $\Delta\emptyset$ is constant.

This implies that other phase contributions are constant and the thickness of the specimen is uniform. With the DFEH method, it is possible to obtain strain maps. The parameters used for the phase reconstruction need to be carefully controlled. The aperture size is one of the most important factors during the inverse Fourier transform of the sideband information. In this case, the (0002) plane diffracted beam is used for the DFEH strain analysis; the reciprocal lattice vectors of GaN and InGaN are g_{GaN}=3.14 nm^{-1}, and g_{InGaN}=3.09 nm^{-1}, respectively. We can estimate the deviation of the diffracted beam as ±0.06 nm^{-1}. This means that the aperture radius used for

phase reconstruction should not be less than 3/50 nm^{-1}. In general, the aperture size was set to reach a position from 1/3 to 1/2 of the distance between the maximums of the center band and the side band; this distance can be increased to improve the spatial resolution. The field of view can be measured and found to be about 2.5 x $10^3 nm^2$, which is larger than that obtained using the HRTEM technique (625 nm^2). The strain map was displayed in Fig. 5.4a where the red color indicates the positive strain value in the InGaN region. The strain profile shown in Fig. 5.4 b. was extracted from the strain map in an area of 3.5 x 9.2 nm^2. The strain measured in the layer varies between 1.8% and 2.25%. As can be seen in the results of the distribution of the lattice spacing in the InGaN and the GaN regions, obtained using the HRTEM technique, the high lattice spacing values at the InGaN surface tend to decrease toward the InGaN/GaN interfaces due to the specimen preparation process, which is relative to the bending of the lattice planes. The DFEH results can be compared to the HRTEM results in terms of the strain value and the depth of strain distribution. From the strain profile shown in Fig. 5.4b, the depth of strain distribution in the InGaN area was calculated, which corresponds to the InGaN MQWs as obtained using HRTEM method.

However, there are also obtained the negative strain, they are - 1 % ~ - 8 %. The negative strain can be present in the GaN barrier and it can be used

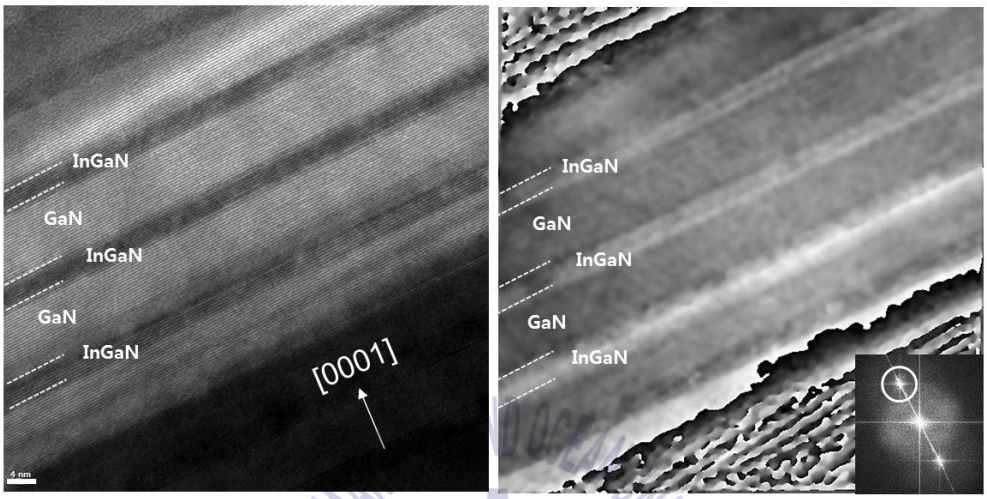

Fig. 5.3 Dark-field image hologram from (0001) diffracted beam shows the biprism position with clear separation, and phase image

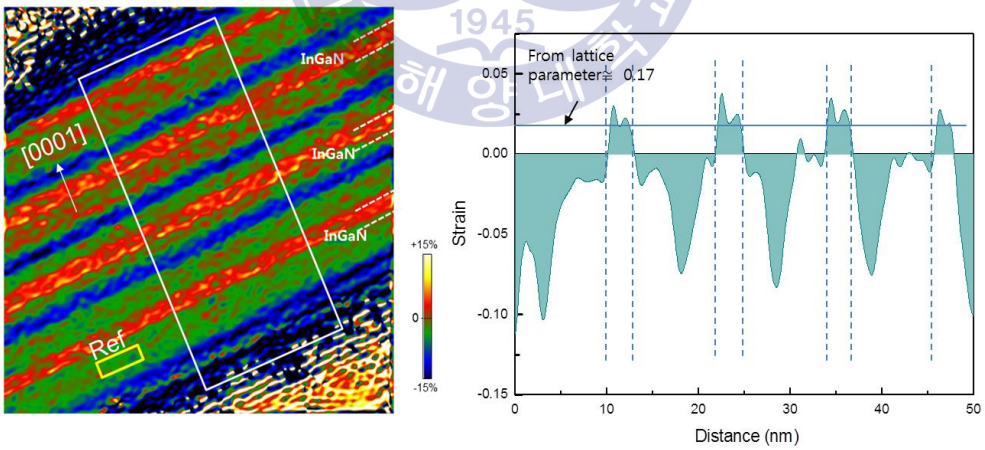

Figure 5.4 Strain mapping image and strain profile

in the strain engineering. But, in our case, the negative strain in the strain map was shown as layer. And the position of negative strain region is not uniform whenever strain measurement. So we think that it is an artifact from overlap by electron beam interaction between MQWs region and reference region which is not clearly due to complex structure of LED.

Nevertheless, DFEH technique has high strain sensitivity, as shown in the TABLE 5.1. Thus it can be a remarkable technique for strain analysis if the problems are solved.

TABLE 5.1 Strain sensitivities by other techniques

Analysis technique	**Sensitivity**
DFEH	0.02 %
NBED	0.06 %
HAADF-STEM	0.15 %

5.3 Summary and Conclusion

In this chapter, the strain of InGaN/GaN MQWs is calculated by DFEH. The strain mapping and distribution was obtained and compared with HRTEM result. The strain values by DFEH were similar to HRTEM result. There are existed the artifact, but the DFEH is expected as an attractive method for strain analysis with its high strain sensitivity.

REFERENCES

[1] S. H. Chae, W. J. Yu, J. J. Bae, D. L. Duong, D. Perello, H. Y. Jeong, Q. H. Ta, T. H. Ly, Q. A. Vu, M. Yun, X. Duan, and Y. H. Lee, *Nature Materials* **12**, 403 (2013)

[2] D. A. Antoniadis,I. Aberg, C. Ní Chléirigh, O. M. Nayfeh, A. Khakifirooz, J. L. Hoyt, *IBM Journal of Research and Development* **50**, 363 (2006)

[3] H. Yin,K. D. Hobart, R. L. Peterson, F. J. Kub, and J. C. Sturm, *IEEE Transactions on Electron Devices* **52**, 2207 (2005)

[4] T. A. Bogetti and J. W. Gillespie, *Journal of Composite Materials* **26**, (1990) 68

[5] A. Tiberj, B. Fraisse, C. Blanc, S. Contreras and J. Camassel, Journal of Physics: Condensed Matter, *J. Phys.: Condens. Matter* **14** , 13411 (2002)

[6] P. F. Fewster and N. L. Andrew, *Thin Solid Films* **319**, 1 (1998)

[7] P. Puech, F. Demangeot, J. Frandon, C. Pinquier, M. Kuball, V. Domnich and Y. Gogotsi, *J. Appl. Phys.* **96**, 2853 (2004)

[8] A. Armigliato, R. Balboni and S. Frabboni., *Appl. Phys. Lett.* **86,** 063508 (2005).

[9] A. Armigliato, A. Spessot, R. Balboni, A. Benedetti, G. Carnevale, S. Frabboni, G. Mastracchio and G. Pavia, *J. Appl. Phys*. **99**, 064504 (2006).

[10] P. Zhang, A. A. Istratov, E. R. Weber, C. Kisielowski, H. He, C. Nelson, and J. C. H. Spence., Appl. Phys. Lett. **89,** 161907 (2006).

[11] K. Usuda, T. Numata, and S. Takagi, *Mater. Sci. Semicond. Process* **8**,

155 (2005).

[12] S. H. Vajargah, M. Couillard, K. Cui, S. G. Tavakoli, B. Robinson, R. N. Kleiman, J. S. Preston and G. A. Botton , *Appl. Phys. Lett*. **98**, 082113 (2011).

[13] E. Guerrero, P. L. Galindo, A. Yáñez, J. Pizarro, M. P. Guerrero-Lebrero and S. I. Molina, *Appl. Phys. Lett*. **95**, 143126 (2009).

[14] A. Béché, J.L. Rouvière, J.P. Barnes, D. Cooper, *Ultramicroscopy* **111**, 227 (2011).

[15] S. Pereira, M. R. Correia, E. Pereira, K. P. O'Donnell, E. Alves, A. D. Sequeira, N. Franco, I. M. Watson and C. J. Deatcher, *Appl. Phys. Lett*. **80**, 3913 (2002).

[16] M. J. Hÿtch, J. Putaux, and J. Pénisson, *Nature* **423**, 270 (2003).

[17] M. Schuster, P. O. Gervais, B. Jobst, W. Hosler, R. Averbeck, H. Riechert, A. Iberl, and R. Stommer, *J. Phys. D: Appl. Phys.* **32**, A56 (1999).

[18] S. Pereira, M. Correia, E. Pereira, K. O'Donnell, E. Alves, A. Sequeira, N.Franco, I. Watson, and C. Deatcher, *Appl. Phys. Lett*. **80**, 3913 (2002)

[19] D. Gabor , Nature **161**, 777 (1948).

[20] H. Lichte, *Ultramicroscopy* **20**, 293 (1986).

[21] A. Orchowski, W.D. Rau, H. Lichte, *Phys. Rev. Lett*. **74**, 399 (1995)

[22] A. Tonomura, T. Matsuda, R. Suzuki, A. Fukuhara, N. Osakabe, H. Umezaki, J. Endo, K. Shinagawa, Y. Sugita, H. Fujiwara, *Adv. Phys.* **41**, 59 (1992) .

[23] R. E. Dunin-Borkowski, M. R. McCartney, D. J. Smith, S. S. P. Parkin, *Ultramicroscopy* **74**, 61 (1998).

[24] T. Denneulin, D. Cooper, J. L. Rouviere, *Micron* **62**, 52 (2014).

Chapter 6 Conclusions

This thesis will suggest analysis methods for InGaN/GaN MQWs in the real LED. This thesis has introduced GaN-based LED as well as InGaN/GaN MQWs which is important region as an active layer and TEM techniques for analysis of InGaN/GaN MQWs. ***In the chapter 3***, a detailed microstructural characterization of a GaN LED chip was carried out using HRTEM and WBDF techniques. Various defects (such as misfit dislocation, stacking faults and voids) were observed near the interfaces of the GaN film and the patterned Al_2O_3 substrate by HRTEM. The results of the determination of dislocation types using the weak-beam dark filed technique shows that most of TDs generated from top surface (TS) turned out to have the edge component. ***In the chapter 4***, A quantitative analysis of In composition in InGaN/GaN MQWs in LED was carried out using high-resolution transmission electron microscopy (HRTEM) and high-angle annual dark-field scanning TEM (HAADF-STEM). The composition was obtained quantitatively by HRTEM and relatively by HAADF-STEM. ***In the chapter***

5, strain in the InGaN/GaN MQWs was analyzed by DFEH. The strain mapping image was obtained and strain distribution was discussed.

As a result, the In composition and strain of InGaN/GaN MQWs were minutely analyzed by TEM techniques of HRTEM, HAADF-STEM, and DFEH. Consequently, this thesis shows that TEM analysis is essential method to obtain detailed information of LED.

Curriculum vitae

Personal brief

Name :	Youngji Cho
Date of Birth :	1987. 3. 28
Nationality :	Korea
Sex :	Female
Address :	958-13 Gwangan3-dong, Suyeong-gu, Busan, 613-810, Korea
Department :	Department of Applied Science
Institution :	Korea Maritime and Ocean University
Position :	Doctor student
Office Address :	#433-1, College of Engineering I, Korea Maritime and Ocean University,727 Taejong-ro, Yeongdo-Gu, Busan, 606-791, Korea
Telephone :	82-51-410-4833
Fax :	82-51-404-3986
E-mail :	choyj0328@gmail.com

Education

2003. 3 ~ 2006. 2

Dukmoon girl's high school

2006. 3 ~ 2010. 2

Bachelor's Degree in department of Nano semiconductor engineering, Korea Maritime and Ocean University, Busan, Korea

(Thesis: Structural and Optical Properties of Thick Film GaN by using Buffer Layer)

2010. 3 ~ 2012. 2

Master's Degree in Department of Applied Science, Korea Maritime and Ocean University, Busan, Korea

(Thesis: A Study on the Reduction of Structural Imperfections in Polar/Non-polar GaN Thick Films Grown by Hydride Vapor Phase Epitaxy)

2012. 3 ~ Present

Doctor's Course in Department of Applied Science, Korea Maritime and Ocean University, Busan, Korea

Academic activities

2008. 5 ~ Present

Research student in Nano Material and Device Laboratory, Korea Maritime and Ocean University, Busan, Korea

2010. 3 ~ 2012. 2

Master student in Department of Applied Science, Korea Maritime and Ocean University, Busan, Korea

2010. 7 ~ 8

Researcher in Matsuoka Laboratory, Institute for Materials Research, Tohoku University, Sendai, Japan

Research Topic : Study on the properties of GaN film grown by MOCVD

2012. 3 ~ Present

Doctor student in Department of Applied Science, Korea Maritime and Ocean University, Busan, Korea

2012. 7 ~ Present

Researcher in Measurement & Analysis Division, National Nanofab Center, Daejoen, Korea

Patent

Jiho Chang, Mina Jung, Jieun Koo, Youngji Cho, "Sterilization system for fluids using ultra violet light sources"

Awards

2009. 11

Award for Best poster presentation, Busan-Ulsan-Keongnam Physical Society

2009. 11

Award for the 5th Busan future scientist, Federation of Busan Science and Technology

2010. 4

Award for Best poster presentation, The Korean Physical Society

2011. 8

Award for Best oral presentation, Society of LED and Solid State Lighting

Grants and Fellowships

2010. 3 ~ 2013. 2

BK21 and allocation fellowship scholarship, Korea Maritime University

"Semiconductor Foundry Service Expert Education Project for Advanced Matine Technology."

2010. 5 ~ 2013. 6

Basic Science Research Program through the National Research Foundation of Korea (NRF) funded by the Ministry of Education, Science and Technology

"A method of growing non-polar nitrides on tungsten carbide deposited on off-angle Si substrate."

2010. 3 ~ 2014.3

ITRC(Information Technology Research Center) support program supervised by the NIPA(National IT Industry Promotion Agency)

"Development of Green IT Technologies based on Fusion of LED-Ocean, Fishery and Shipbuilding Industry.

2012. 8 ~ 2013.5

Advanced Technology Center for Information Electronic Materials & Components

Experience of Equipment and materials

1. Thin film growth
   A. Thermal evaporators and furnaces
   B. Ultra high vacuum sputter
2. Characterization
   A. Scanning electron Microscopy (Operation & Analysis)
   B. Atomic force microscopy (Operation & Analysis)
   C. Photoluminescence (Operation & Analysis & Maintenance)
   D. Hall effect measurement (Operation & Analysis)
   E. Cathodoluminescence (Analysis)

F. High resolution X-ray diffraction and simulation (Operation & Analysis)

G. Transmission electron microscopy (Operation & Analysis)

i. TEM and STEM imaging

ii. Diffraction pattern analysis

(Indexing program : PhIDO, Simulation program : xHREM)

iii. STEM simulation (Simulation program : xHREM)

iv. EELS

v. TEM electron holography (+ DFEH)

3. Materials

A. Structural, optical and electrical properties of GaN thick films

B. Structural, optical and electrical properties of non-polar GaN thick films

C. Structural properties of GaN/InGaN MQWs LED

D. Structural properties of graphene

E. Structural, optical properties of AlON powder

F. Structural properties of ITO powder

Achievements

A. International publications

1. Youngji Cho, Jun-Seok Ha, Mina Jung, Hyun-Jae Lee, Seunghwan Park, Jinsub Park, Katsushi Fujii, Ryuichi Toba, Samnyung Yi, Gyung-Suk Kil, Jiho Chang, Takafumi Yao, " The impact of an intermediate temperature buffer on the growth of GaN on an AlN template by hydride vapor phase epitaxy", **Journal of Crystal Growth**, 312 (2010) 1693

2. Seungjun Oh, Mina Jung, Jieun Koo, Youngji Cho, Sungkuk Choi, Samnyung Yi; Gyungsuk Kil, Jiho Chang, “The mechanism of ZnO nanorod growth by vapor phase transportation”, **Physica E**, 42 (2010) 2285

3. Youngji Cho, Sungkuk Choi, Gyung-Suk Kil, Hyun-Jae Lee, Takafumi Yao, Jun-Mo Yang, JunghoYoo, Jangwoo Kwon, Jiho Chang, “Effects of the inclination direction of vicinal m-plane sapphire substrates on the crystal quality of m-plane GaN film”, **Journal of Crystal Growth**, 325 (2011) 85

4. Yujin Cho, Jieun Koo, Youngji Cho, Woong Lee, Jeungwoo Lee, Byeongwoo Lee, Sangtae Lee, Jiho Chang, “Synthesis of AlON materials for UV emitting devices”, **Physica Status Solidi (c)**, 10 (2013) 861

5. Jieun Koo, Seunghwan Park, Woong Lee, Youngji Cho, Hyojong Lee, Sangtae Lee, and Jiho Chang, “High Performance Printed Ultraviolet-Sensors Based on Indium–Tin-Oxide Nanocrystals”, **Japanese Journal of Applied Physics**, 52 (2013) 115001

6. Do Van Lam, Sang-Min Kim, Youngji Cho, Jae-Hyun Kim, Hak-Joo Lee, Jun-Mo Yang and Seung-Mo Lee, “Healing defective CVD-graphene through vapor phase treatment.” **Nanoscale,** 6 (2014) 563

7. Youngji Cho, Jiho Chang, Joonseok Ha, Hyun-jae Lee, Katsushi Fujii, Takafumi Yao, Woong Lee, Takashi Sekiguchi, Jun-Mo Yang and Jungho

Yoo, “Threading Dislocation Reduction in a GaN Film with a Buffer Layer Grown at an Intermediate Temperature”, **Journal of the Korean Physical Society**, 65 (2014) 214

8. Youngji Cho, Jun-Mo Yang, Do Van Lam, Seung-Mo Lee, Jae-Hyun Kim, Kwan-Young Han, Jiho Chang "Transmission Electron Microscopy Specimen Preparation for Layer-area Graphene by a Direct Transfer Method" **Applied Microscopy**, 44 (2014) 133

9. Youngji Cho, Jung Sik Park, Jun-Mo Yang, Kyung Jin Park, and Yun Chang Park, Jiho Chang, Sang Geul Lee, Kwan-Young Han, "Quantitative compositional analysis of InGaN/GaN multiquantum wells in light-emitting diodes," **Journal of Materials Research**, 30 (2015) 2893

10. Van Vuong Hoang, Young Ji Cho, Jung Ho Yoo, Jun-Mo Yang, Sungha Choi, Wooduck Jung, Yong Ho Choi, Soon-Ku Hong, "2D strain measurement in sub-10 nm SiGe layer with dark-field electron holography", **Current Applied Physics**, 15 (2015) 1529

B. Domestic publications

1. 김 홍 승, 김 아 라, 이 주 영, 장 보 라, 김 홍 승, 조 영 지, 장 낙 원, "수열합성법으로 성장된 산화 아연 나노 막대의 성장 시간에 따른 구조적, 광학적 특성", 새물리, 60 (2010) 359

2. 조영지, 이현재, 이웅, T. Sekiguchi, T. Yao, 양준모, 유정호, 장지호, "성장모드가 HVPE GaN 후막의 결함 형성에 미치는 영향", 한국해양대학교 부설 산업기술연구소, 28 (2011) 77

3. 조유진, 조영지, 유진엽, 구지은, 최성국, 장지호, 이상태, 이원재, "열처리를 통한 (11-20) ZnO 기판의 표면 형상 및 광학적 특성의 변화에 대한 고찰", 새물리, 61 (2011) 311

4. 구지은, 조영지, 장지호, 박승환, 이웅, 이효종, 이상태, "고온가압 열처리법을 이용한 ITO 의 전기적 특성 개선과 가스센서 응용에 관한 연구", 새물리, 61 (2011) 311

5. 구지은, 조영지, 장지호, 박승환, 이웅, 이효종, 이상태, "산소분압제어를 통한 ITO 박막의 고온열처리방법에 대한 연구", 새물리, 62 (2012) 61

6. 조영지, 유정호, 양준모, 박동용, 김종균, 최강보, 장지호, “저온분사법에 의해 제조된 Cu-Ga 타겟의 스퍼터링 특성평가”, 분말야금학회, 23 (2016) 21

C. Presentations in the international conferences

1. Jiho Chang, Hyunjae Lee, Mina Jung, Youngji Cho, Bonheun Koo, Bonheun Koo, Hyojong Lee, Takafumi Yao, “Growth of O- and Zn-polar ZnO films by DC magnetron sputtering”, International Symposium on Compound Semiconductors, June, 2010.

2. M. N. Jung, S. K. Choi, J. E. Koo, Y. J. Cho, S. N. Yi, G. S. Kil, S. T. Lee, H. J. Lee, T. Yao, d. C. Oh, J. H. Chang, “Decrease of Aluminum concentration during the synthesis of Al-doped ZnO nanostructures at high temperature”, International Coference on Molecular Electronics and Devices, May, 2010.

3. Jiho Chang, Mina Jung, Hyunjae Lee, Youngji Cho, Yujin Cho, JinyeopYoo, Sungguk Choi, Takafumi Yao, “Growth and characterization of single crystalline Zn-polar ZnO films by sputtering for the application to a template for GaN”, International Workshop on Znic Oxide and Related Materials, August, 2010.

4. Youngji Cho, Hyun-Jae Lee, Woong Lee, Takashi Sekiguchi, Takafumi Yao, JunghoYoo, Jun-mo Yang, Jiho Chang, “The role of an intermediate temperature buffer in the improvement of crystallinity of HVPE GaN,”, The 15th International Symposium on the Physics of Semiconductors and Applications, July, 2011

5. Youngji Cho, Joonseok Ha, Hyun-Jae Lee, Takafumi Yao, Woong Lee, Takashi Sekiguch, Ryuichi Toba, Jun-Mo Yang, Jungho Yoo, Jiho Chang, “The role of an intermediate temperature buffer on the improvement of crystallinity of HVPE GaN”, The 72nd Autumn Meeting of the Japan Society of Applied Physics, August, 2011

6. Youngji Cho, Junseok Ha, Hyeonjae Lee, Katsushi Fujii, Takafumi Yao, Woong Lee, Takashi Sekiguchi, Jun-Mo Yang, Jungho Yoo, Jiho chang, “Reduction of threading dislocation density in a thick GaN films with an intermediate temperature buffer layer”, The 16th International Conference on Metal Organic Vapor Phase Epitaxy, May, 2012

7. Youngji Cho, Sungkuk Cho, Soohoon Jung, Hyunjae Lee, Dongcheol Oh, Jiho Chang, “The effect of substrate pre-treatment on the quality of homoepitaxial GaN films growth by Gas Source-MBE”, 29th North American Molecular Beam Epitaxy Conference (NAMBE), October, 2012

8. Yang Jun-Mo, Youngji Cho, Park Kyung-Jin, Park Chang Yun, Jungho Yoo, Jeong Seong Chil, “Quantitative analysis of the strain and composition in $In_xGa_{1-x}N$ MQWs”, The 69th Annual Meeting of the Japanese Society of Microscopy, May, 2013

9. Y. J. Cho, J. S. Park, J.-M. Yang, K. J. Park, Y. C. Park, J. H. Yoo, C. S. Jeong, S. G. Lee, J. H. Chang, “Quantitative compositional analysis of the $In_xGa_{1-x}N$/GaN multi quantum wells in LEDs”, The 11th International Nanotech Symposium & Nano-Convergence Expo, July, 2013

10. Youngji Cho, Jun-Mo Yang, Do Van Lam, Sang-Min Kim, Jae-Hyun Kim, Yun Chang Park, and Jiho Chang, "Morphology and Structural Graphene Analysis by Low Voltage TEM", M&M conference 2014

D. Presentations in the Domestic conferences

1. 조영지, 정미나, 주미연, 김시영, 구지은, 하준석, 이현재, 박승환, 박진섭, YAO Takafumi, TOBA Ryuichi, 장지호, “AlN template 상의 Hydride Vapor Phase Epitaxy 를 이용한 GaN 성장 시 중간층의 역할에 관한 연구” 한국물리학회 봄 학술발표대회, 2009 년 4 월.

2. 조영지, 정미나, 장지호, 이현재, 하준석, “HVPE 법으로 GaN 성장 시 버퍼 층의 유무에 따른 박막 내 잔류 응력의 차이에 관한 고찰”, LED 반도체 조명학회, 2009 년 10 월

3. 오승준, 조영지, 김시영, 구지은, 정미나, Kensho Okamoto, 장지호, “LED-LED 광•전 하이브리드 통신시스템의 구현”, 2009 LED 반도체 조명학회, 2009 년 10 월

4. 조영지, 정미나, 이현재, 하준석, Takafumi Yao, 장지호, “HVPE 법으로 GaN 성장시 버퍼층의 유무에 따른 후막의 결정성 변화에 관한 연구”, 한국물리학회 부산경남울산지부 제 54 회 학술발표회, 2009 년 12 월

5. 조영지, 정미나, 이현재, 최성국, Takafumi Yao, 이웅, 장지호 “성장양식의 변화에 따른 HVPE 로 성장한 GaN 의 특성 변화에 관한 연구”, 한국물리학회 봄학술발표대회, 2010 년 4 월

6. 장지호, 조유진, 조영지, 구지은, 최성국, 정미나 " C-plan 과 A-plan bulk ZnO 기판의 발광 특성의 차이에 관한 연구”, 한국물리학회 봄학술발표대회, 2010 년 4 월

7. 최성국, 조영지, 이현재, T. Yao, 한주섭, 길경석, 장지호, “HVPE growth of m-plane GaN on vicinal surface sapphire substrates”, LED, 반도체 조명학회 국내학술대회, 2010 년 8 월

8. 조유진, 최성국, 조영지, 이웅, 이병우, 이상태, 장지호, “스크린 프린팅 방법으로 제작한 전계방출형 발광소자의 UV 발광특성에 대한 연구”, LED, 반도체 조명학회 국내학술대회, 2011 년 8 월

9. 조영지, 하준석, 이현재, Katsuchi Fujii, Takafumi Yao, 이웅, Takashi Sekiguchi, 양준모, 유정호, 장지호, “중간 온도에서 성장한 버퍼층을 이용한 HVPE GaN 후막 내 결함 밀도의 감소 방법에 대한 연구”, LED, 반도체 조명학회 국내학술대회, 2011 년 8 월

10. 조영지, 최성국, 이현재, Katsushi Fujii, Takafumi Yao, 이웅, Takashi Sekiguchi, 양준모, 유정호, 장지호, “The growth of m-plane HVPE GaN film on vicinal surface sapphire substrates, LED, 반도체 조명학회 국내학술대회, 2012 년 2 월

11. 조영지, 양준모, 박중식, 박경진, 박윤창, 유정호, 정칠성, 장지호, “HAADF-STEM 기법을 이용한 $In_xGa_{1-x}N$ MQW 내 In 조성의 정량적 분석”, 한국현미경학회 추계학술대회, 2012 년 11 월

12. 조영지, 양준모, 박중식, 박경진, 박윤창, 유정호, 정칠성, 장지호, “고분해능 TEM 영상을 이용한 $In_xGa_{1-x}N$ MQWs 내 구조 및 In 조성의 정량적 분석”, 한국현미경학회 춘계학술대회, 2013 년 6 월

13. 조영지, 양준모, Do Van Lam, 이승모, 김재현, 박윤창, 장지호, “저전압 TEM 측정을 이용한 그래핀 구조 분석”, 한국현미경학회 추계학술대회, 2013 년 11 월

14. 조영지, 양준모, 박경진, 유정호, 장지호, “고분해능 TEM 과 암시야 전자홀로그래피를 이용한 InxGa1-x N MQWs 내 In 조성 및 격자변형의 정량적 분석” 한국반도체학술대회, 2015 년 2 월

감사의 글

본 논문을 마무리 하며 그 동안의 박사과정 생활 동안 감사했던 분들께 인사 드립니다. 많은 분들의 도움이 있었기에 길고 힘들었던 박사 과정을 이겨낼 수 있었던 것 같습니다.

오랜 시간동안 한결같이 보살펴주시고 지도해주신 장지호 교수님께 정말 감사하다는 말씀 드리고 싶습니다. 그 동안 부족한 모습을 많이 보여드렸음에도 항상 저를 격려해 주셔서 어려울 때도 힘을 낼 수가 있었습니다. 나노 반도체 공학과의 이삼녕 교수님, 안형수 교수님, 양민 교수님, 김홍승 교수님과 늘 학과의 많은 일을 하시는 이봉춘 조교님께 감사의 말씀을 전하고 싶습니다. 그리고 논문 심사에 도움을 주신 안지훈 교수님, 김정창 교수님께도 감사 말씀 올립니다.

대전에서 제가 박사 논문을 쓸 수 있게 도움주신 나노종합기술원의 양준모 박사님. 바쁘신데도 신경 많이 써주셔서 언제나 감사하고 있습니다. 실험 할 때 많은 것을 가르쳐주신 유정호 박사님과 박윤창 선임님, 그 외에 저에게 친절하게 대해주신 나노종합기술원의 특성평가실 분들께 감사드리고 싶습니다.

자주 못 보지만 늘 한결 같은 친구들, 혜리, 크로쓰 멤버들 예서, 수경, 소연, 유정, 유진 항상 챙겨주고 신경 써주는 경희 언니랑 형부, 우현이 오빠, 만나면 늘 즐거운 별시 동생들, 다들 제게 보내주는 관심과 사랑에 감사 인사 전합니다. 마지막으로 사랑하는 가족들 착한 동생 봉근이, 늘 뒤에서 받쳐주시는 어머니, 삶의 기쁨이 되어버린 귀여운 딱지와 깐쵸, 묵묵히 도와주시는 아저씨 덕분에 무사히 박사 과정을 끝낼 수 있었던 것 같습니다.

여러분들이 저에게 주신 모든 사랑과 관심에 걸 맞는 사람이 될 수 있도록 언제나 노력하고 정진하겠습니다. 모두에게 다시 한 번 감사인사 드립니다.